

The Impact of Surface Normals on Appearance

Kathleen Dorothy Moore

Hanson, Massachusetts

Bachelor of Arts, College of the Holy Cross, 2009
Master of Science, College of William and Mary, 2011

A Dissertation presented to the Graduate Faculty
of the College of William and Mary in Candidacy for the Degree of
Doctor of Philosophy

Department of Computer Science

The College of William and Mary
August 2016


APPROVAL PAGE


This Dissertation is submitted in partial fulfillment of
the requirements for the degree of


Doctor of Philosophy

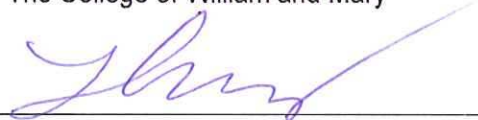

Kathleen Dorothy Moore

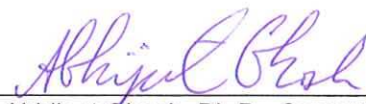
Approved by the Committee, May 2016


Committee Chair
Assistant Professor Pieter Peers, Computer Science
The College of William and Mary


Associate Professor Peter Kemper, Computer Science
The College of William and Mary


Assistant Professor Xu Liu, Computer Science
The College of William and Mary


Associate Professor Gang Zhou, Computer Science
The College of William and Mary


Abhijeet Ghosh, Ph.D., Computer Science
Imperial College London

ABSTRACT

The appearance of an object is the result of complex light interaction with the object. Beyond the basic interplay between incident light and the object's material, a multitude of physical events occur between this illumination and the microgeometry at the point of incidence, and also beneath the surface. A given object, made as smooth and opaque as possible, will have a completely different appearance if either one of these attributes - amount of surface mesostructure (small-scale surface orientation) or translucency - is altered. Indeed, while they are not always readily perceptible, the small-scale features of an object are as important to its appearance as its material properties. Moreover, surface mesostructure and translucency are inextricably linked in an overall effect on appearance. In this dissertation, we present several studies examining the importance of surface mesostructure (small-scale surface orientation) and translucency on an object's appearance.

First, we present an empirical study that establishes how poorly a mesostructure estimation technique can perform when translucent objects are used as input. We investigate the two major factors in determining an object's translucency: mean free path and scattering albedo. We exhaustively vary the settings of these parameters within realistic bounds, examining the subsequent blurring effect on the output of a common shape estimation technique, photometric stereo. Based on our findings, we identify a dramatic effect that the input of a translucent material has on the quality of the resultant estimated mesostructure. In the next project, we discuss an optimization technique for both refining estimated surface orientation of translucent objects and determining the reflectance characteristics of the underlying material. For a globally planar object, we use simulation and real measurements to show that the blurring effect on normals that was observed in the previous study can be recovered. The key to this is the observation that the normalization factor for recovered normals is proportional to the error on the accuracy of the blur kernel created from estimated translucency parameters.

Finally, we frame the study of the impact of surface normals in a practical, image-based context. We discuss our low-overhead, editing tool for natural images that enables the user to edit surface mesostructure while the system automatically updates the appearance in the natural image. Because a single photograph captures an instant of the incredibly complex interaction of light and an object, there is a wealth of information to extract from a photograph. Given a photograph of an object in natural lighting, we allow mesostructure edits and infer any missing reflectance information in a realistically plausible way.

TABLE OF CONTENTS

Acknowledgments	iii
Dedication	iv
List of Tables	v
List of Figures	vi
1 Introduction	2
2 Background	5
2.1 Bidirectional Reflectance Distribution Function (BRDF)	5
2.2 Types of BRDFs	6
2.3 Image Formation	10
2.4 Bidirectional Subsurface Scattering Reflectance Distribution Func- tion (BSSRDF)	12
3 Impact of Translucency on Normal Estimation	21
3.1 Motivation	22
3.2 Background	23
3.3 Prior work	28
3.4 Empirical Study	29
3.5 Conclusion	40
4 Normal Estimation Refinement	42
4.1 Prior Work	43

4.2	Background	44
4.3	Project Overview	47
4.4	Results	52
4.5	Discussion & Limitations	53
4.6	Conclusion	55
5	Image-Based Microgeometry Manipulation	56
5.1	Prior Work	57
5.2	Background	59
5.3	System Overview	63
5.4	Results	70
5.5	Discussion & Limitations	72
5.6	Conclusion	73
6	Conclusion	78

ACKNOWLEDGMENTS

Pieter, thank you for taking me on and guiding me through the multi-dimensional world of computer graphics. Your accessibility will go unmatched, your mastery of the field - supreme, and your love of good teaching will be my benchmark, whether or not I end up teaching. I am grateful to have this lifelong connection in learning with you.

Thank you, also, to my committee. I have great respect for your experience and knowledge and am honored to have my work vetted by you.

I would like to offer special thanks to Dr. Bo Dong, my research partner and good friend. I have missed you in my last year at the College. Thank you for diving into problems with me and laughing whenever possible.

To the rest of the graphics group: thank you for being a friendly and supportive bunch. Keep going, study hard.

This work was supported in part by the U.S. National Science Foundation under grants IIS-1350323 and IIS-1016703.

Even when I missed out on so much, working on my degree 454 miles away, my family supported me in numerous ways. I would like to dedicate this dissertation to them - especially to my Dad, who pressed me with questions on a regular basis and who is now finding answers, along with me, in my heart.

LIST OF TABLES

4.1 BSSRDF parameters estimated using the joint multi-channel deconvolution versus ground truth parameters.	55
---	----

LIST OF FIGURES

2.1	A sampling of diffuse (a, c, f); specular (e, g, h); and glossy (b, d, i) BRDFs from Matusik et al. [35].	7
2.2	Diagram of diffuse reflectance. Incident light from direction ω_i hits the surface and scatters in all directions.	8
2.3	Underneath the surface of a translucent material, light scattering from direction ω_i and hitting surface point x_i incurs a number of scattering "events" within the medium before exiting at some other point x_o and traveling in direction ω_o	13
2.4	A photon scattered from a translucent surface can either exit immediately at the point of entry via surface reflectance ("s.r."), scatter once before exiting as single-scattering ("s.s") or undergo multiple scattering ("m.s.") before exiting.	14
2.5	The direction of scattering is dictated by the phase function, p , and the general scattering direction is dictated by the mean cosine parameter, g . Left: backward, $g = -1.0$, Center: isotropic, $g = 0.0$, Right: forward, $g = 1.0$	17
3.1	Sample input to the photometric stereo algorithm - Top: A sphere lit from three different lighting directions and photographed from the same viewpoint. Bottom: RGB-encoded normals calculated for the sphere.	24
3.2	Simulated image of a Lambertian, sinusoidal surface illuminated from three different directions by a directional light source.	27

3.3	Simulated image of a translucent, sinusoidal surface illuminated from three different directions by a directional light source.	27
3.4	The ground truth normal map employed in our simulations. The sample size is $10cm^2$, and the amplitude of the sinusoidal normal variation is $\frac{\pi}{2}cm$. The inset shows the false-color coding of the normals.	31
3.5	The average angular error plot for photometric normals computed from observations under three directional light sources, and for multiple scattering only, without taking Fresnel transmittance into account (i.e., $\eta = 1.0$) for scattering albedo $\alpha \in [0.1, 1.0]$ and mean free path $l_d \in [0.35, 6.5]$	33
3.6	The impact of varying mean free path (vertical axis) on a slice from the normal map. As mean free path increases, the features in the normal map gradually become blurred out.	34
3.7	A comparison of $\frac{F_t(\omega_{iz}, \eta)max(0, \omega_{iz})}{F_{t0}}$ for varying indices of refraction. . .	35
3.8	The average angular error plot for photometric normals computed from observations under three directional light sources, and for multiple scattering only, with varying index of refraction $\eta \in \{1.1, 1.3, 1.5\}$, for scattering albedo $\alpha \in [0.1, 1.0]$ and mean free path $l_d \in [0.35, 6.5]$	36
3.9	The average angular error plot for photometric normals computed from observations under three directional light sources, and for multiple scattering and single scattering (i.e., $\eta = 1.3$) with the mean cosine $g \in \{-0.5, 0.0, +0.5\}$, for scattering albedo $\alpha \in [0.1, 1.0]$ and mean free path $l_d \in [0.35, 6.5]$	37

3.10	The average angular error plot for photometric normals computed from observations under four directional light sources, and for multiple scattering only, with $\eta = 1.3$, scattering albedo $\alpha \in [0.1, 1.0]$ and mean free path $\in [0.35, 6.5]$	38
3.11	Left: Photometric normals estimated from a translucent soap sample. Note how multiple scattering blurs out most surface details compared to the multiple+single scattering photometric normal map. Further observe the effect of the wavelength dependent diffuse reflectance R_d on the sharpness of the photometric normals. Right-top: a cross-polarized captured image, exhibiting only multiple sub-surface scattering, used to compute the multiple scattering photometric normals. Right-middle: polarization difference image showing the specular surface reflectance and single scattering removed by cross polarization. Right-bottom: unpolarized photograph of the translucent soap, showing both reflectance due to multiple as well as single scattering.	39
4.1	The predominant signal that is convolved by the blurring effect of subsurface scattering, is incident irradiance and its interaction with the surface normal at the point of incidence, x_i . Thus, outgoing Fresnel transmission at the point x_o can be considered independently of the blurring operation.	45
4.2	Results of photometric stereo computed from images of a hand illuminated in infrared, red, green, blue, and ultraviolet light.	47
4.3	A flow chart of the ground truth surface normal and translucency parameter estimation algorithm. Overall, the error metric, $\ L - L_{est}\ _2$, is minimized via the Hooke and Jeeves method.	50

4.4	(a) Ground truth surface normals captured directly from the mold used to cast the normal variation on the pink soap material (i). (b-d) Naively applying photometric stereo directly on the observations yields blurred normals. (f-g) Result from our method computed on each channel separately. (e) Result from joint optimization on all color channels simultaneously. (j-l) Corresponding ground truth and recovered BSSRDF profiles.	53
4.5	Result for Cheddar Cheese (i). For this example, no ground truth normals are available. (b-d) Naively applying photometric stereo directly on the observations yields blurred normals. (f-g) Result from our method computed on each channel separately. (e) Result from joint optimization on all color channels simultaneously. (j-l) Corresponding ground truth and recovered BSSRDF profiles.	54
5.1	Mug illuminated with distant light. Image courtesy: [8].	60
5.2	Example of a captured irradiance environment map [9].	62
5.3	Left: Example of a rendered, glossy sphere input, which had been masked with the computed normals; however, hallucinated pixels remain around the rim. Right: Improved input, the edge of which has been eroded to remove the halo around the rim. Rendering: Mitsuba [28].	65
5.4	Progression of reflected radiance map "inflation" depicted as a convex hull generated from surface normal points input to the system. The inflation begins with the original input (left) and iterates, subdividing triangles and projecting points to the hull, to arrive at the final inflation (right.) Rendering: Blender [5].	67

5.5	Left: Original natural image input; Top-Right: Original collected reflectance radiance map for hemisphere (green plastic ball). Bottom-Right: Interpolated result to which novel surface normal directions can be attributed.	67
5.6	Examples of stamps (depicted as surface normals encoded in RGB) in the system: waves, bumps, random (within a hemisphere of angles), and a concave dimple, respectively. (Not pictured but also available: blurring and sharpening.)	68
5.7	Screenshots of the editing application. Top: initial editing window, on which the user selects a region to edit. Middle: Editing tool pop-up menu. Bottom: The stamping sub-menu.	74
5.8	Top-Left: Surface normals of rendered, diffuse object. Top-Right: Object illuminated by environment map. Bottom-Left: Original input. Bottom-Right Object stamped with waves, which bend around the corner. Rendering: Mitsuba [28].	75
5.9	Interpolated reflected radiance map for the brown, diffuse object. Note the black spots scattered throughout, due to the high-frequency shadowing introduced by the object's self-shadowing geometry. . .	75
5.10	Top-Left: Original input of a velveteen bag, inset is a close-up of the original crimped region. Top-Right: Dimple stamp applied to flat portion of input, causing an apparent impression in the surface. Bottom-Left: Dimple stamp also applied to crimp in the bag neck. Notice how the crimping is preserved underneath. Bottom-Right: Dimple applied to the same region on the crimp, this time without global illumination scaling factor. Notice the excessive shadowing introduced.	76

5.11 Top-Left: Original input of a pink, cotton sock. Top-Right: Bump stamp applied to flat portion of input, causing apparent bumps in the surface. Bottom: Bump stamp also applied to ridge of sock. . .	76
5.12 Left: Original input of a glossy peapod figure. Right: Dimple stamp applied to input. Notice that the depth-edge is included in the depression, as well as the shadowing associated with such a discontinuity.	76
5.13 Left: Original input of crumpled ball of aluminum. Right: Dimple stamp applied to input. Notice that the underlying, complex geometry is still preserved.	77
5.14 The blue bag exhibits a fold or ridge (left) that is not detected in the normals (right.)	77

The Impact of Surface Normals on Appearance

Chapter 1

Introduction

As our eyes pan around a room, our brains are performing a rapid classification process: "That's a shiny chair; that's a cardboard coffee sleeve; that's an orange flower pot." If we were to take this data as input to computer-aided design software, the appearance of these objects would probably translate as lacking. What we would have failed to represent is the *woven* fabric chair, the *corrugated* cardboard coffee sleeve, and the *ceramic* orange flower pot. The realism is in the details - in this case, the microgeometry. Fine aberrations on the surface of an object compound, resulting in a richness that does not go unnoticed by our visual system. Because of this, we seek to highlight the importance of capturing and fully making use of microgeometric information in the digital capture and representation of appearance.

One can look at the geometry of objects in two ways: locally or globally. On the whole, we recognize large changes in the overall geometry of an object as its shape. It is this synthesis of three-dimensional information that enables us to make mental leaps at assessing an object's identity or function. On a smaller scale, however, we may never really notice the small aberrations on the surface of an object. If we do, we may have had to touch it, hold it very closely to our eyes, or see it interact with another surface. Physical effects like light transmission, friction and gravity may help to reveal the small-scale texture or detail on an object.

What happens when we take microgeometric information for granted? If we try to recreate objects that exhibit such detail, this lack of cohesion between physics and the object itself may become much more noticeable. We have seen how sensitive humans can be at detecting irregularities in the digital rendering of human faces (a phenomenon known as the "uncanny valley.") On its own, the microgeometry of an object may be imperceptible to us. We are usually made aware of sub-millimeter inaccuracies of an object either through rigorous measurement and validation or by our perceptual system's prowess at recognizing physical implausibilities.

It is important to try to estimate the surface orientation of objects as well as possible, irrespective of an object's level of translucency, gloss, or placement in a scene. Fields such as medicine and anthropology often rely on accurate recordings of object shape and reflectance for records. The entertainment industry also strives for fine manipulation of object geometry, especially after they have rigorously captured this data from a real-world scene. Yet, inaccuracies in shape estimation and object reflectance continue to persist due to constraints on time, data, or technology.

On an even larger scale, digitally rendered scenes present numerous challenges in the context of microgeometric complexity. The subtle undulation of an object's surface may greatly impact, for instance, the refraction of light cast through its translucent form and onto a nearby surface. The color of one translucent object may interreflect with that of another. Shadow edges can become harder or softer depending on the level of detail and properties of the light grazing an object. Inject numerous light sources and complex shapes into a scene, and the interactions among objects and physical phenomena become multitudinous.

When the estimates for surface shape are inaccurate, the resultant inconsistencies in appearance can be traced down to the particle-level of an object. Overall appearance of a material is directly tied to two factors: geometry and reflectance. An interesting topic continues to be the role of error in geometric information and its greater impact in relation to all visual phenomena in a scene and appearance. This has become our area of interest.

In the rest of this text, we explore the effects of surface orientation accuracy on appearance in various ways. First, we take a common shape estimation algorithm and present it with more realistic input - input that violates its rigid assumptions - and examine the results in a regimented, empirical study. Following this, we introduce a method for refining the result of the previous output. Finally, we introduce an image editor that engages the user with the mesostructure of an object, permitting the user to alter the underlying surface normals and obtain an updated reflectance image. The entirety of this work is an examination of the impact of surface normals on object appearance, and it reveals the diversity of information that awaits in a single photograph of an object.

Chapter 2

Background

Differences between objects at the particle-level have direct ties to the performance of the methods used to acquire objects' geometry. For the purposes of assessing which methods to use, it is imperative to understand what type of material is at hand. The material properties of objects range from diffuse to specular, opaque to translucent - and in combinations of these properties. In the following section, we establish the basis for the descriptions of light transport and material reflectance, and we define the techniques and models that are used repeatedly throughout our experimentation.

2.1 Bidirectional Reflectance Distribution Function (BRDF)

Describing the appearance of a material begins with describing the interaction of incident light and the surface of the material. We make use of the bidirectional reflectance distribution function (BRDF) to make this distinction [40]. However, to understand the concept of a BRDF, we must first understand the intuition behind the quantities "radiance" and "irradiance." Radiance stems from radiant power (flux.) While flux measures energy flow through a surface for a period of time, irradiance measures this incident flux *on* a surface, per unit surface area (with units of watts/m^2 .) Similarly, radiance (measured in $\text{watts/steradian}\cdot\text{m}^2$) is a way of expressing how much power arrives at or leaves from a

surface point in terms of solid angle and unit projected area. Solid angle is the surface area of a unit sphere that is encompassed by the projection of an object (or area) from the center of the unit sphere to the surface of the unit sphere.

The BRDF of a material is the ratio of its differential exitant radiance (dL) to differential incident irradiance (dE) at a point x_i . It can also be thought of as the ratio of differential exitant radiance to incident irradiance, L_i modulated by the angle between the surface normal n_{x_i} (surface direction at that point) and the incident light direction, ω_i . The BRDF has units sr^{-1} (steradians⁻¹). The formulation of the BRDF is shown in Eq. 2.1:

$$f_r(x_i, \omega_i, \omega_o) = \frac{dL_o}{dE} = \frac{dL_o}{L_i(\omega_i \cdot n_{x_i})d\omega_i}. \quad (2.1)$$

This 4D function is defined at a point x_i on the surface for a pair of incident ω_i and exitant ω_o lighting directions. The value of a BRDF is always positive, and can vary, per material, per wavelength. Whether or not one interchanges the incident and exitant directions, however, the value of the BRDF will remain the same - an example of what is termed "Helmholtz reciprocity." A BRDF is a powerful, technical descriptor of material appearance.

A more intuitive definition of the BRDF would be that it represents the portion of incident light that reflects off the surface of a material, for a particular direction. The outgoing directionality of the reflected light is dependent on the underlying material. The BRDF is a canonical model upon which more complex material reflectances are characterized. It is also just one component of a larger system that describes all of the light transport in a scene and thus the entirety of the image formed within the human brain, a camera, or any other light-sensor.

2.2 Types of BRDFs

There are special classes of BRDFs under which we can organize many materials: specular, diffuse, and glossy. Diffuse BRDFs describe reflection of light that is uniform over

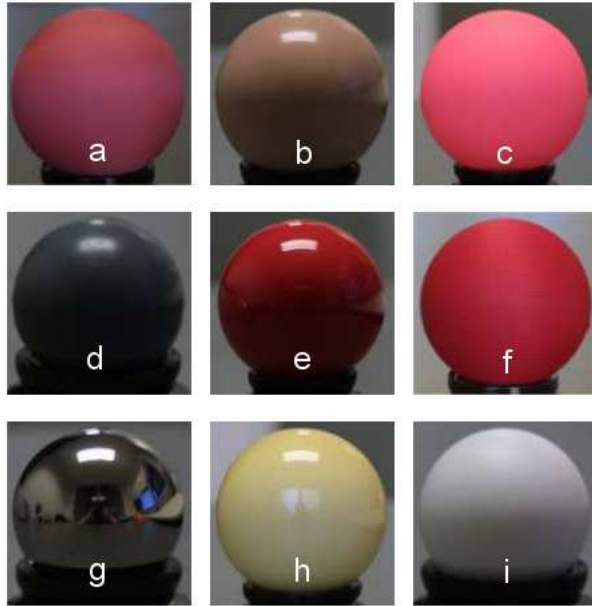


Figure 2.1: A sampling of diffuse (a, c, f); specular (e, g, h); and glossy (b, d, i) BRDFs from Matusik et al. [35].

the whole hemisphere of directions. Specular BRDFs describe the reflection of light in a single direction only. Glossy BRDFs describe reflection that is a combination of these responses, focused at a small solid angle around the mirror (specular) direction. Together, these generalized BRDF characterizations comprise many types of material reflectances, as shown in Fig. 2.1.

Diffuse BRDFs

For materials that are diffusely reflecting, or, “Lambertian,” the value of the BRDF is independent of outgoing direction, as light is isotropically scattered. In Fig. 2.2 we illustrate incident light on a diffuse material that is then reflected in all directions over the hemisphere.

Since light is distributed uniformly in all outgoing directions for the diffuse BRDF, the reflectance of the surface will look the same from any vantage point. This type of reflectance is a limit-case, in that it presents an idealized material that does not allow light

to penetrate the surface and exit at another point, nor can the light undergo any amount of absorption at the particle-level. Consequently, a tight coupling of incident irradiance to exitant radiance is maintained. In other words, the point of incidence is equal to the point of exitance. One can see this from Lambert's model for the diffuse BRDF:

$$f_r(x_i, \omega_i, \omega_o) = \frac{\rho}{\pi}, \quad (2.2)$$

where ρ , the reflectance or, "albedo", can take on any value from 0 to 1 but remains constant for the entire hemisphere in this special case of a BRDF.

The strong assumption of a Lambertian material underlies many methods that seek to estimate the surface orientation of objects. This type of material, however, is far from the reality of the composition of everyday materials.

Specular BRDFs

A specular BRDF is, in other words, a mirror-BRDF. In this case, illumination from each direction ω_i , incident on this surface, is reflected into a particular reflected direction ω_o , depending on the surface normal at the incident point, n_{x_i} . Specifically, ω_o forms the same angle with n_{x_i} that ω_i does, which is called the "mirror direction." The formal description of the formation of ω_o is shown in Eq. 2.3. Consequently, this reflected energy will only be seen if the view direction aligns with this reflected direction, and when the surface normal direction is exactly halfway between the incoming irradiance direction and the reflected direction.

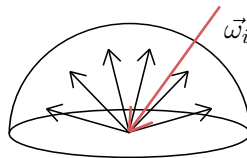


Figure 2.2: Diagram of diffuse reflectance. Incident light from direction ω_i hits the surface and scatters in all directions.

$$\omega_o = 2(\omega_i \cdot n_{x_i})n_{x_i} - \omega_i \quad (2.3)$$

Once it is determined that a material exhibits some degree of specularity, it is important to incorporate the controlling effect of the Fresnel equations into the BRDF. The Fresnel equations utilize the indices of refraction of two different media that meet at the material's surface, and calculate the portion of light that is reflected from the surface and what portion (may be) transmitted into the surface.

Fresnel transmission is comprised of two equations, shown in Eq. 2.4 and Eq. 2.5, where θ_i is the angle between n_{x_i} and ω_i .

$$F_{ts} = 1 - \left| \frac{\eta_1 \cos \theta_i - \eta_2 \sqrt{1 - \left(\frac{\eta_1}{\eta_2} \sin \theta_i\right)^2}}{\eta_1 \cos \theta_i + \eta_2 \sqrt{1 - \left(\frac{\eta_1}{\eta_2} \sin \theta_i\right)^2}} \right|^2 \quad (2.4)$$

$$F_{tp} = 1 - \left| \frac{\eta_1 \sqrt{1 - \left(\frac{\eta_1}{\eta_2} \sin \theta_i\right)^2} - \eta_2 \cos \theta_i}{\eta_1 \sqrt{1 - \left(\frac{\eta_1}{\eta_2} \sin \theta_i\right)^2} + \eta_2 \cos \theta_i} \right|^2 \quad (2.5)$$

Eq. 2.4 is the formulation for Fresnel transmission that dictates transmissivity for light that is polarized perpendicularly to the plane of incidence, and Eq. 2.5 is the formulation for the parallel analog. Because together, Fresnel transmission and reflection conserve energy, each of F_{ts} and F_{tp} can also be calculated from polarized Fresnel reflectance components $1 - F_{rs}$ and $1 - F_{rp}$, respectively. Usually, the final transmission term, F_t , is calculated as the average of F_{ts} and F_{tp} . This is valid, assuming that the incoming illumination is fully unpolarized. In both equations, ω_i is the angle of incident illumination, ω_t is the angle of the refracted (transmitted) ray, η_1 is the index of refraction of the first medium, and η_2 is the index of refraction of the second, through which the transmission is occurring.

Glossy BRDFs

Glossy BRDFs fall somewhere between diffuse and specular BRDFs. There are different ways of modeling these BRDFs. They can be considered the result of a specular BRDF that has undergone a change in surface roughness. In this case, microgeometric perturbations roughen the surface at a local scale but preserve the global smoothness of the object. Thinking of this another way, this formulation is essentially a specular BRDF with a "blurred" reflectance. This would form a cone or lobe, of specularity. However, glossy surfaces can also be the result of multi-layered materials that are diffuse or specular.

One could think of glossy materials as being the sum of diffuse and specular components, in a more theoretical sense. In the Phong BRDF model [42], reflectance is the weighted sum of a diffuse and specular component. This model is not physically-based, however; it is purely empirical because its parameters have no basis in physical characteristics. There are many different models that simulate gloss with many different methods.

Most shiny materials are glossy and not specular because they are not perfect reflectors of light in the canonical specular formulation. Like specular reflection, however, the shape of the specular lobe of a glossy material is still dependent on incident light direction, making the glossy BRDF sensitive to complex light interactions.

Within a scene, the illumination bouncing off of the various surfaces of objects creates a complex scenario of light transport. Each recursive bounce of light that is sensed by the eye or a camera is the result of all of its previous interactions with materials. It helps to consider this situation in a more formal way.

2.3 Image Formation

Light is electromagnetic energy that, when it enters a scene, can reveal forms, reflect material color, and encounter numerous scattering and absorption events in its travel through space. A succinct way of describing the entirety of the radiance leaving each

point in a scene, due to the multitudinous events of light transport at any given instant is through Kajiya's rendering equation [30]. This equation, Eq. 2.6, which outputs the observed radiance, L_o at a surface point, x , incorporates the BRDF but also other scene conditions that impact the appearance of any given point in the scene.

$$L_o(x_i, \omega_o, \lambda, t) = L_e(x_i, \omega_o, \lambda, t) + \int_{\Omega} f_r(x_i, \omega_i, \omega_o, \lambda, t) L_i(x_i, \omega_i, \lambda, t) (\omega_i \cdot n_{x_i}) d\omega_i. \quad (2.6)$$

The BRDF is important to include in this model because it characterizes the distribution of reflected radiance at the point in question. However, the format of most terms is defined in a more explicit formulation that includes the wavelength, λ , and point in time, t , in which the illumination is occurring. The reason behind this formulation is that the rendering equation provides the radiance that is observed in a scene, at a specific point, at the precise moment, and for the exact wavelength of the electromagnetic spectrum that is originally hitting the scene. This could vary across the electromagnetic spectrum and through time. The result is a composition of all light interactions up to that moment that exits at the point x in a certain direction, ω_o . Because of this, the incoming reflectance information is integrated over the entire hemisphere, Ω .

The next term in the integration is, L_i , which represents the amount of incident irradiance from direction ω_i that is hitting the surface at point x_i . This illumination may carry with it the interactions of one or more surfaces elsewhere in the scene, so it is important to incorporate it into the reflected radiance at this instant in time.

As we touched on before, surface orientation is easily described as a vector called a "normal": the direction that is perpendicular to a tangent plane at that point on the surface. The inner product, $(\omega_i \cdot n_{x_i})$, the last term in the integration, is the cosine of the angle between the surface normal at point x_i and each incident lighting direction. This inner product is commonly known as the "foreshortening" term: incident irradiance at that point on the object is proportional to this clamped (positive) cosine. We see this cosine

in Eq. 2.1, the BRDF model. This factor also underlies the shading differences across a surface with varying geometry. Hence, it is a modulator on reflectance and the incoming irradiance.

Lastly, if the surface emits its own light at x_i , an additional term for emitted radiance, L_e , is added to the total radiance. Light sources are, themselves, components of a scene, so they are accounted for in this term. The rendering equation is non-trivial to solve in its entirety for each point in a scene but many rendering techniques vary in the approximations made to speed up the computation. For instance, the techniques of path tracing and photon mapping use a Monte Carlo technique to stochastically arrive at a solution. Despite the rendering equation's high degree of fidelity to physics, it is technically too simple to fully describe all visual effects, especially subsurface light transport.

The above model for light transport in a scene is a simplified case of the full range of light scattering that is possible in the world. It does not account for complex light effects, such as diffraction (when the wavelength of light is roughly the same size or larger than an orifice that it hits), or polarization-specific effects, among other phenomena. One common effect is that of subsurface light scattering. In this case, a photon will scatter or be absorbed after an inestimable number of interactions with particles in a translucent object's substrate. This characteristic of light interaction with translucent objects is a phenomenon that plays a significant role in the rest of our work and frames the rendering equation as a special case of a more robust scattering model.

2.4 Bidirectional Subsurface Scattering Reflectance Distribution Function (BSSRDF)

Light that penetrates the surface of a material at certain point will undergo subsurface scattering. In this case, light that enters at point x_i will exit the surface not only at that same point as surface reflectance, but likely at any other possible surface point, x_o . This

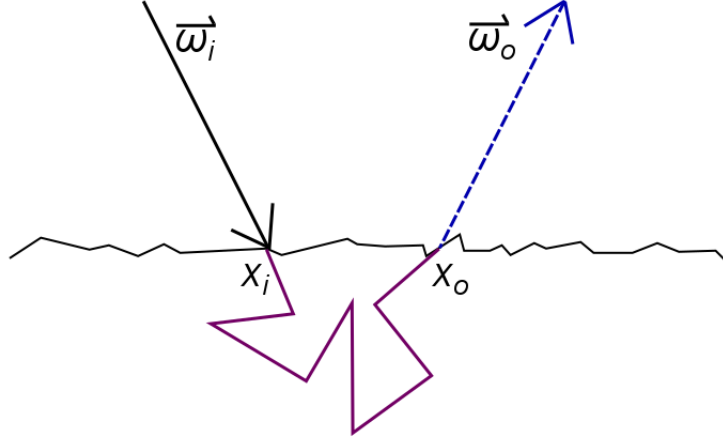


Figure 2.3: Underneath the surface of a translucent material, light scattering from direction ω_i and hitting surface point x_i incurs a number of scattering "events" within the medium before exiting at some other point x_o and traveling in direction ω_o .

subsurface scattering is depicted in Fig. 2.3.

Between the points of entrance and exit, both scattering and absorption events can occur at the particle level. Underneath the surface, there can either be one scattering event before the particle exits through the surface (single scattering) or more than one scattering event (multiple scattering), as shown in Fig. 2.4 Each type of scattering is modeled slightly differently in practice, i.e. when simulating subsurface light transport. Together, these events are known as subsurface scattering.

For rendering purposes, the outgoing radiance of a translucent material can be calculated similarly to the rendering equation, Eq. 2.6, but allowing for volumetric scattering. Notice the dependence on the outgoing position introduced by volumetric scattering. The analytical formulation in Eq. 2.7 integrates over both incident position (area) and direction (incident illumination angle):

$$L_o(x_o, \omega_o) = \int_A \int_{\Omega} S(x_i, \omega_i, x_i, \omega_o) L_i(x_i, \omega_i) (\omega_i \cdot n_{x_i}) d\omega_i dA(x_i). \quad (2.7)$$

The subsurface diffusion portion of the integral, S , can be described analytically by the bidirectional subsurface scattering reflectance distribution function (BSSRDF), an 8D

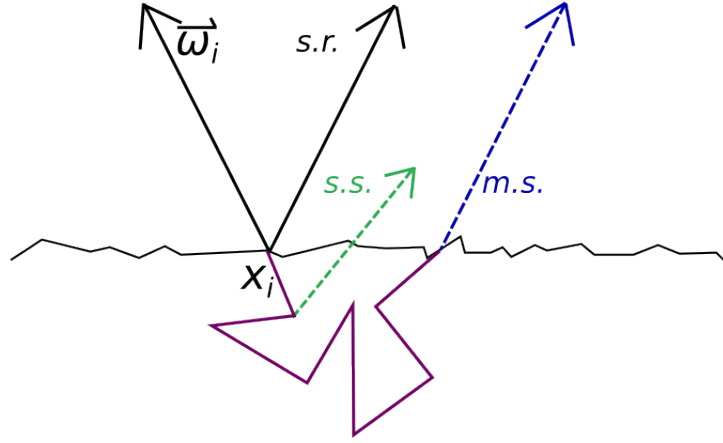


Figure 2.4: A photon scattered from a translucent surface can either exit immediately at the point of entry via surface reflectance ("s.r."), scatter once before exiting as single-scattering ("s.s") or undergo multiple scattering ("m.s.") before exiting.

function [40] over incident position x_i , outgoing position x_o , incident direction ω_i and outgoing direction ω_o :

$$S(x_i, \omega_i; x_o, \omega_o) = S^1(x_i, \omega_i; x_o, \omega_o) + S^d(x_i, \omega_i; x_o, \omega_o), \quad (2.8)$$

in which S^1 and S^d comprise the single- and multiple scattering components of the full subsurface light transport. The multiple scattering component of subsurface light transport is generally considered to be a diffusion process [45], leading to the development of many models that approximate subsurface light transport.

Multiple Scattering

The diffusive portion of subsurface scattering is known as "multiple scattering." A photon in the process of multiple scattering is undergoing successive scattering "events." An event could be either one of absorption or of scattering, denoted by the coefficients, σ_a and σ_s , respectively. The absorption coefficient signifies the rate at which the photon would lose radiant flux due to absorption by an encountered particle; the scattering coefficient is similar. Taken together, the entirety of the photons comprising a beam of

light undergo these events with varying probability and a certain distribution of possible scattering directions, dictated by the medium through which the photons are traveling.

One way of modeling the multiple scattering phenomenon is with diffusion theory. In a diffusion approximation of multiple scattering, the assumption is made that the material at hand is a homogeneous and semi-infinite slab. In Jensen et al. [29], a detailed explanation of a diffusion approximation for multiple scattering is given, and it includes several key points underlying the intuition behind the diffusion approximation for multiple scattering, including:

- The scattering profile of a highly scattering medium tends to be isotropic.
- The direction of the flux of irradiance is from high density to low.

The particular analytical model for the diffusion approximation is described well in Jensen et al. [29]; with additional conditions in place, the model can be adjusted to work within the physical boundaries of a homogeneous medium. For complex shapes (non-slabs), however, the diffusion approximation decreases in reliability as a model, as geometric idiosyncrasies interfere with the pattern of fluence in the medium. For small or slowly varying regions, however, the diffusion approximation acts as a relatively accessible, albeit simplified, estimation of the scattering profile of a beam of light through a translucent medium.

Multiple scattering, S^d , is formulated as follows:

$$S^d(x_i, \omega_i; x_o, \omega_o) = \frac{1}{\pi} F_t((\omega_o \cdot n_{x_o}) R_d(||x_i - x_o||) F_t((\omega_i \cdot n_{x_i}), \eta), \eta), \quad (2.9)$$

in which n_x is the surface normal at position x , $R_d(||x_i - x_o||)$ is the diffuse reflectance describing the subsurface transport from point x_i to x_o , and each F_t is a Fresnel transmission term with index of refraction η , one for incident illumination, one for exitant illumination. As mentioned previously, the Fresnel terms dictate the proportion of light that is reflected or transmitted through an interface between differing media. Rendering only the multiple

scattering contribution with incident illumination from a single direction, Eq. 2.7 can be simplified as Eq.2.10:

$$L(x_o, \omega_o) = \frac{1}{\pi} \int_A F_t((\omega_o \cdot n_{x_o}), \eta) R_d(||x_i - x_o||) F_t((\omega_i \cdot n_{x_i}), \eta) L_i(x_i, \omega_i) (\omega_i \cdot n_{x_i}) dx_i, \quad (2.10)$$

There are two, key parameters to any model describing subsurface light transport. The first parameter is "scattering albedo," which is defined as: $\alpha = \frac{\sigma_s}{\sigma_s + \sigma_a}$, the ratio of the scattering coefficient, σ_s over the sum of this scattering coefficient and the absorption coefficient, σ_a . This sum in the denominator is also known as the "extinction coefficient," which is often denoted as σ_t . The other parameter is called the "mean free path," or l_d . Mean free path is defined as: $l_d = \frac{1}{\sigma_s + \sigma_a}$. Together, scattering albedo and mean free path dictate the magnitude and extent of the diffusion of subsurface light transport, respectively. A mathematical model for describing translucency should incorporate these parameters in some way because the scattering and absorption coefficients are tied to the physical properties of each translucent material.

The scattering direction of photons through a translucent material can be largely backwards, out of the surface of the material and in the hemisphere of directions centered on ω_i , isotropic, forwards, in the hemisphere of directions opposite ω_i , or somewhere within this range. This distribution of likely directions is known as the "phase function," $p(g, \omega_i' \cdot \omega_i')$, given in terms of the mean cosine $g \in [-1, +1]$, and the refracted incident and outgoing directions ω_i' and ω_o' respectively.

The phase function is integral to a description of translucency because it dictates the overall scattering "lobe" of the particles. The mean cosine, g , itself dictates whether single scattering is mostly forward, into the material ($g = 1.0$), mostly isotropic ($g = 0$), or backwards, out of the material ($g = -1.0$). These types of scattering profiles are illustrated in Fig. 2.5.

In our analysis, we employ the dipole-diffusion approximation for R_d [29], introduced

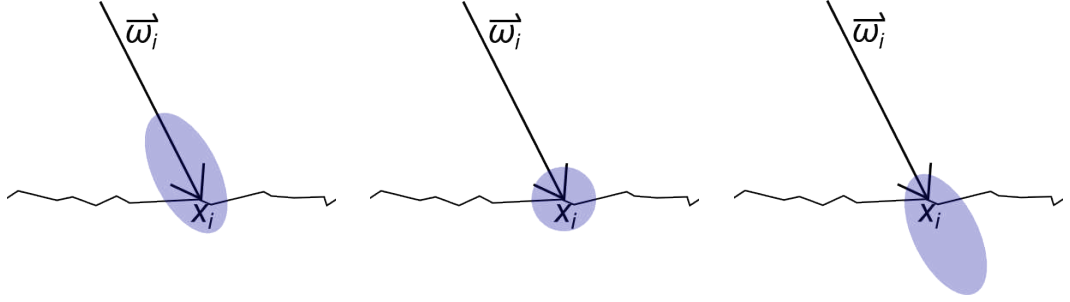


Figure 2.5: The direction of scattering is dictated by the phase function, p , and the general scattering direction is dictated by the mean cosine parameter, g . Left: backward, $g = -1.0$, Center: isotropic, $g = 0.0$, Right: forward, $g = 1.0$

by Jensen et al., which is an approximation of subsurface diffusion for globally planar, homogeneous materials such as milk, wax, or marble, calculated in line with the normal direction at a point on the surface of the object. R_d provides the means of photon diffusion underneath the surface - the "scattering profile." The idea of the dipole diffusion model is to embed two hypothetical point light sources above and below the scene for which one is trying to simulate diffusion. The modeling of the fluence between these "positive" (lower) and "negative" (upper) light sources for all incoming light source directions results in the dipole diffusion model, the analytical formulation for which R_d is shown in Eq. 2.11:

$$R_d = \frac{\sigma'_s}{4\pi(\sigma'_s + \sigma_a)} \left[(\sigma_{tr}d_r + 1) \frac{e^{-\sigma_{tr}d_r}}{\sigma'_t d_r^3} + z_v(\sigma_{tr}d_v + 1) \frac{e^{-\sigma_{tr}d_v}}{\sigma'_t d_v^3} \right]$$

in which,

$$\sigma'_s = \sigma_s(1 - g)$$

and

$$\sigma'_t = \sigma'_s + \sigma_a$$

(2.11)

The coefficient σ_{tr} is the effective transport coefficient (a measure of the rate of diffusion in the medium,) d_r is the distance between our point of incidence x_i and the light source,

and d_v is the distance between x_i and either of the virtual light sources that hypothetically sit near the boundary of the surface. The purpose of using "reduced" versions of coefficients, such as σ'_t , the reduced extinction coefficient, is to incorporate the potential anisotropy introduced by g , the mean free path.

One could substitute any of the applicable diffusion models for R_d . For instance, the dipole model has been extended to account for multiple layers [12]. More recently, the quantized diffusion model [10] was developed to better approximate subsurface light transport for a wider range of materials but approximating the two-dimensional diffusion profile as a sum of Gaussians. It can also simulate diffusion from an oblique (non-normal) direction by offsetting the centers of the Gaussians used. Building upon this approach, Habel et al.'s [21] photon beam diffusion model is able to approximate diffusion (also at oblique angles) more efficiently than the former. Instead of incorporating diffusion approximation through a sum of Gaussians, this process is replaced by Monte Carlo simulation with incorporated importance sampling. The benefit of choosing one of these latter models is that they account for diffusion at non-normal directions, and thus are more appropriate for non-slab, rough surfaces. For simple cases of translucency on a plane and didactic examples, the standard dipole model is sufficient. To describe the translucency of curved or more geometrically complex surfaces, quantized or photon beam diffusion are more appropriate.

Single Scattering

Because the distance traveled by a particle that undergoes single scattering is often not far from the point of incidence, single scattering is usually approximated using a BRDF. A popular model for single scattering is that of Hanrahan and Krueger [22], which can be substituted for the single scattering S^1 term:

$$f_r^1(x, \omega_i, \omega_o) = \alpha F \frac{p(g, \omega_i' \cdot \omega_o')}{|(n_{x_o} \cdot \omega_i')| + |(n_{x_o} \cdot \omega_o')|}, \quad (2.12)$$

where α is the scattering albedo, and F is the product of the incident and exitant transmission terms F_t . Since single scattering is often approximated as a BRDF; it is also considered as not breaking the assumption that incident irradiance is tightly coupled to exitant radiance. While not exactly Lambertian, if g is largely backscattering, single scattering can have an approximate Lambertian behavior for a large range of incident directions. The mean cosine, g , and index of refraction, η , are of particular importance to study within the context of single scattering as their values can vary widely in real-world materials.

Lowering Dimensionality

The unique feature of subsurface scattering as a whole is that, through the diffusion process, the angular distribution of outgoing radiance becomes disconnected from the incident irradiance direction. While both single and multiple scattering are generated as functions of incident and exitant light direction, the observed effect is ambiguous. Therefore, the observed radiance from a translucent material can be written as the sum of the exitant radiance due to single scattering L^1 and the exitant radiance due to multiple scattering L^d :

$$L(x_o, \omega_o) = L^1(x_o, \omega_o) + L^d(x_o, \omega_o). \quad (2.13)$$

The above simplification is possible due to the linearity of light transport, the phenomenon that the combined effect of lighting in a scene is equal to the sum of the individual effects of the light sources. The benefit is that this process can be simplified to a 4D problem from an 8D problem, one that is irrespective of incident light direction, ω_i .

Overall, one could think of subsurface scattering as pseudo-diffuse behavior, since each light particle travels rather erratically underneath the surface of the material, again independent of a particular incident light direction. The problem occurs when incident light intersecting any given point on the surface can contribute to exitant radiance at another point. This characteristic violates the terms of Lambertian reflectance and disconnects

incident irradiance from exitant radiance [45]. Many shape estimation algorithms assume a tight relationship between incident and exitant radiance. Consequently, the common presence of subsurface scattering in materials renders these materials potentially unusable in these algorithms.

Chapter 3

Impact of Translucency on Normal Estimation

Countless materials at hand exhibit some degree of translucency, such as skin, fruit, milk, jade, and the list goes on. It is tempting to apply photometric stereo to objects constructed from these materials despite the fact that they do not comply with the assumed material standards, because it is such a simple procedure. To determine the extent to which the result of photometric stereo [48], a popular shape-estimation algorithm, degrades in the presence of translucent input, we have executed an empirical study using both simulation and data from a real capture.

According to theory, the photometric stereo technique should not hold for non-Lambertian materials. In the following project, published in [36] we investigate the range of accuracy in results from photometric stereo when it is applied to arbitrarily translucent materials. We seek to confirm our expectations that for a widely-used technique, the applicability of photometric stereo is limited.

3.1 Motivation

Digitally reproducing the appearance of physical objects is a difficult and important problem in computer graphics and computer vision. Both shape and reflectance need to be accurately characterized in order to obtain a faithful reproduction. While modern geometry acquisition techniques are capable of achieving sub-millimeter accurate results [25], these methods make no guarantees on the accuracy of the resulting surface normal. However, accurate surface normals are important to faithfully reproduce surface reflectance. A practical solution is to directly acquire surface normals that are then subsequently used to augment the high resolution geometry [39].

In this study, we empirically investigate the impact of violating the assumption of coupled incident and exitant radiance on the accuracy of photometric stereo. In other words, we evaluate its accuracy on translucent materials. We perform simulations based on Jensen et al.'s [29] dipole-diffusion model and compute the accuracy of photometric stereo as a function of mean free path, scattering albedo, mean cosine of the phase function, and number of light source directions. Our analysis shows that the ratio of geometric feature size versus mean free path and single scattering play an important role, whereas the other parameters influence the error less. We demonstrate the validity of our analysis on a physical material sample.

To the best of our knowledge, the relation between the coupling of incident and exitant radiance has not yet been explored in the context of photometric stereo. With the ever-increasing drive for higher resolution geometry, understanding this relation and its impact on the accuracy of photometric stereo becomes critical as materials that at low or moderate resolution appear diffuse, can exhibit subsurface light transport when examined at a finer resolution.

3.2 Background

In the process of creating a digital representation of an object, we often need to photograph or scan an object quickly, and as accurately as possible, capture its geometry and reflectance. There may not always be room for a scanner or imposing gantry in the acquisition area. For just an estimation of the surface orientation of the visible points of the object, how can we do this quickly and in a small amount of space?

A general technique is "shape-from-shading": shading information in the photograph of an object is used as input to an algorithm that then infers surface orientation from shading differences, which present themselves as foreshortening, or cosine falloff term. One such enduring version of this technique is the photometric stereo method for computing surface orientation [48]. The goal of this method is to obtain an estimate of the surface normal, at each pixel, of a target object. It is important to note that, for Lambertian reflectance, foreshortening does not depend on the viewing angle but only on the angle between the incident lighting direction and the surface normal direction.

Using photographs of the object taken from the same vantage point, photometric stereo calculates the surface normal at each visible point of the object, discretized per pixel. Fig. 3.1 shows sample input images and the final, photometric stereo output of the landscape of three-dimensional normals of a sphere, in which the normals are encoded in red, green, and blue (RGB) values. A change horizontally in red, indicates a change in the x-direction, a change vertically in green is a change in the y-direction, and a change in depth, or the z-direction, is a change in blue.

The algorithm assumes that the illumination in each input image is a single, directional light source. For a light source to be "directional," the rays emanating from the source must be parallel. Illumination of this kind is difficult to achieve in practice. Hence, it is assumed that the target object is sufficiently smaller than the light source. Notice that the amount of input images in Fig. 3.1 is three. This is not an arbitrary number. The amount of input images must be greater than or equal to the dimensionality of the surface normals

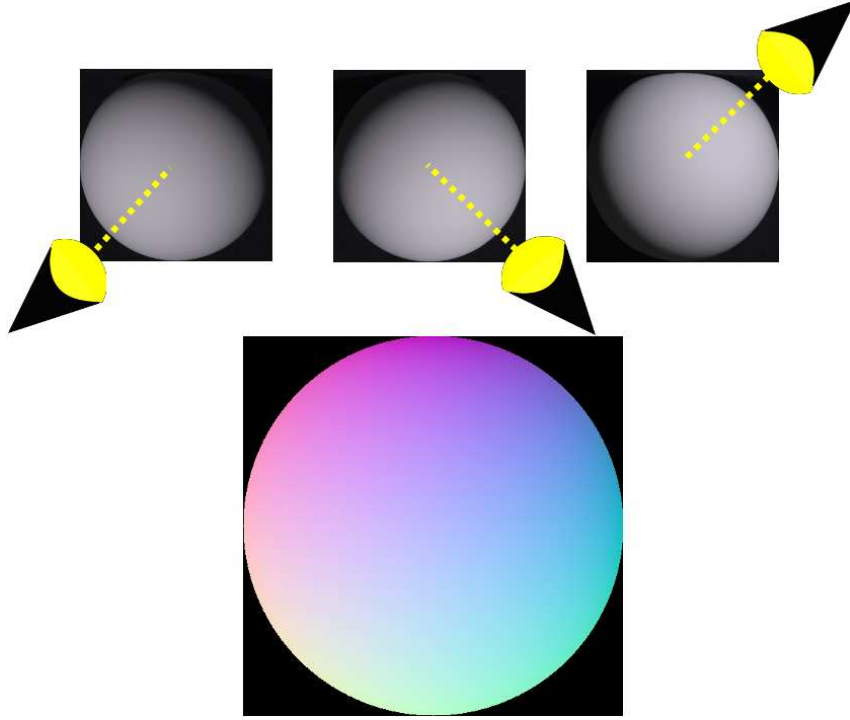


Figure 3.1: Sample input to the photometric stereo algorithm - **Top:** A sphere lit from three different lighting directions and photographed from the same viewpoint. **Bottom:** RGB-encoded normals calculated for the sphere.

for which the algorithm is solving, which is typically three dimensions for this image-based algorithm. The radiance intensity at each pixel of these u input images can be formulated as:

$$l = \frac{\rho}{\pi}(n \cdot d), \quad (3.1)$$

in which n is the unnormalized normal, d is the light source direction, and l is resultant radiance image. The foreshortening term appears again in this equation, causing the shading variation over the surface of the target object. Returning to the full collection of input images then, we have:

$$\begin{aligned}
l_1 &= \frac{\rho}{\pi}(n_1 \cdot d_1) \\
l_2 &= \frac{\rho}{\pi}(n_2 \cdot d_2) \\
l_3 &= \frac{\rho}{\pi}(n_3 \cdot d_3), \\
. &= . \\
. &= . \\
. &= . \\
l_u &= \frac{\rho}{\pi}(n_u \cdot d_u),
\end{aligned}$$

a linear system of equations. For the three unknowns of the three-dimensional surface normal, we need three input images that contain the known radiance (intensity) values, and their associated three lighting directions. (Lighting directions can be obtained by capturing a Lambertian sphere under the appropriate light sources and solving for them, since the normals of a sphere are known.) We can concatenate all of this information into a single linear system as shown in Eq. 3.2 to solve for all of the surface normals for which there is an intensity value, using the least squares method.

$$L = \frac{\rho}{\pi}(N \cdot D) \quad (3.2)$$

L is a $1 \times u$ matrix of radiance values observed, per photograph, under one of u known light source directions $D = [d_1, d_2, d_3 \dots d_u]$ (a $3 \times u$ matrix). Each column in D represents an individual incident lighting direction, representing the illumination in one photograph. N is a $u \times 3$ matrix of the unknown values for all surface normals. The final step is to normalize the normals returned in N to remove the effect of ρ , thus calculating the traditional output of photometric stereo.

Photometric stereo is a lightweight method for capturing surface normals of an object in that it requires little data as input, commonplace acquisition equipment, and little processing time. In all, a minimum of only three photographs of the target object is required to solve the system of equations for each surface normal. It is this ease-of-use,

however, that is routinely abused because virtually zero real-world objects have perfectly diffuse reflectance because they exhibit some degree of translucency, or subsurface light transport. The validity of inferring shading information from differences in foreshortening only holds as long as all incident light is reflected from the same point at which it makes contact with the surface, which is not true with translucent materials. Therefore, to some degree, one is usually violating the assumptions made by the photometric stereo method.

Because it is so straightforward, the photometric stereo method is ubiquitous. Our first goal was to characterize the degree of accuracy achieved by the photometric stereo method for calculating surface normals of translucent objects. With this information, we could characterize the degree to which the major parameters dictating translucency have an effect on the results.

The idea of the simulated, empirical study is to have full control over all variables in a typical photometric stereo setup, including presenting the method with its ideal input. With full control, we can vary the parameters of translucency for our simulated material and ensure that for each independent variation, the rest of the parameters remain the same.

Photometric stereo is supposed to be ideal for "smooth surfaces with few discontinuities." To push these assumptions to the limit, we design a simulated target input: a globally smooth, sinusoidal surface. The overall texture of the surface is smooth, but there is surface normal variation to measure. However, there are no sharp discontinuities in the variation, and the surface remains the same throughout the simulation, irrespective of its level of translucency.

The "ground truth" surface normals are computed from the surface with Lambertian material qualities. The test surface with approximate illumination positions and exhibiting the Lambertian material is shown in Fig. 3.2. It is important to note how light position is important, as the center and right images of Fig. 3.2 are virtually identical. We were careful to position lights so that the surface would show intensity variation for at least three of the input images, to be able to calculate the surface normals.

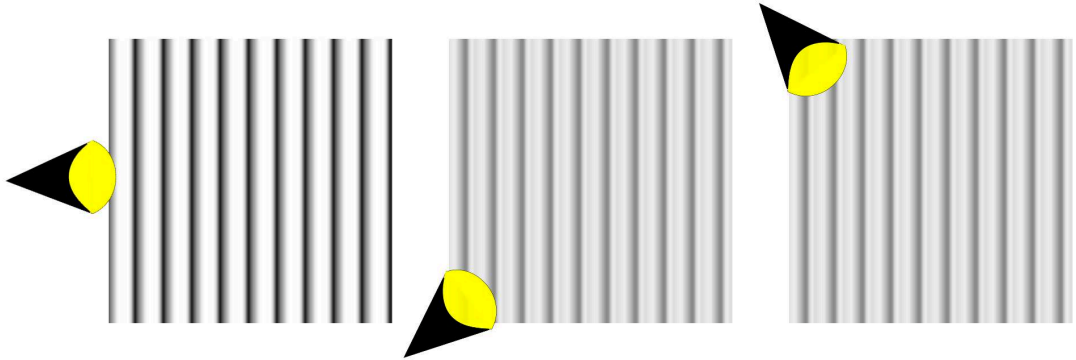


Figure 3.2: Simulated image of a Lambertian, sinusoidal surface illuminated from three different directions by a directional light source.

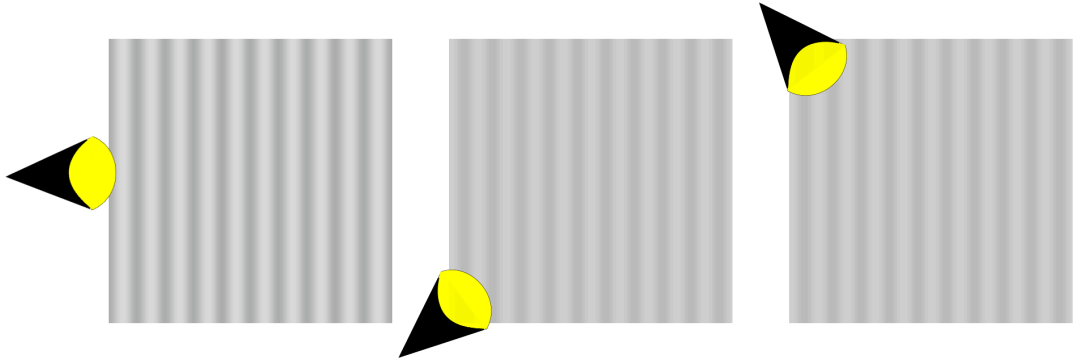


Figure 3.3: Simulated image of a translucent, sinusoidal surface illuminated from three different directions by a directional light source.

By varying the two main parameters that dictate translucency, scattering albedo, α , and mean free path, l_d , we can create an arbitrarily translucent surface. In Fig. 3.3, one can see an example of the same illuminated surface, but with non-Lambertian settings, exhibiting a degree of translucency.

Even with the human eye, it is apparent that there is a significant difference in the appearance of the surface as its illuminated. The contours of the surface appear less sharp in the translucent version than in the Lambertian version. This is a key observation that underlies not only the intuition behind this empirical study - that subsurface scattering confounds the incident illumination signal and introduces error in the result of photometric

stereo - but also further work in this dissertation. Next, we discuss the simulation setup in more specific terms.

3.3 Prior work

While not widely applicable in its original manifestation, photometric stereo has since been extended and generalized to handle, among other singularities, shadowing, specularities, and general surface reflectance. Since its inception, several variants have been proposed that extend photometric stereo to handle more general lighting conditions (e.g., [37, 4]), shadows (e.g., [3]), non-Lambertian reflectance (e.g., [20, 1]), etc. Ma et al. [34] exploit differences in polarization behavior of illumination to estimate photometric normals, and observe that there is a discrepancy between so-called "diffuse" and "specular" normals and conclude that this is due to interreflections and subsurface scattering. None of the above has analyzed the impact of the different parameters of subsurface scattering on the accuracy of photometric stereo.

Capturing geometry for translucent objects has long been a recognized problem in computer graphics. Goden et al. [18] elaborated on the difficulty by measuring the bias in depth measurements of marble under laser range scanning. Of course, if one is able to coat a translucent surface with a diffuse material, the problem is avoided. Goesele et al. [19] demonstrate the effectiveness of this approach by "dusting" a translucent object with a diffuse powder to circumvent the problem of subsurface scattering. This is not always possible, as objects might be malleable or fragile. We want to assume that any target object for which its geometry needs to be acquired must be touched as little as possible. Thus, reflectance from multiple scattering is exposed.

Given the fact that reflectance from multiple scattering is the source of unreliability in shape estimation techniques, some have tried to isolate it from direct reflectance when taking measurements. For example, Nayar et al. [38] use high-frequency, sinusoidal illumination patterns to separate direct from multiple-scattered illumination. Furthermore,

Holroyd and Lawrence [24] formally analyze the applicability and expected error of using this separation technique on optical triangulation methods. In a similar vein, Ma et al. [34] use a spherical gradient illumination pattern to isolate direct surface reflection from subsurface scattering information. Single scattering is, of course, nearly direct reflection in practice. Recognizing this, Inoshita et al. [27] have reconstructed the shape of a translucent object by only looking at the single scattering component. Unfortunately, it is difficult to separate single scattering from specular reflection. In our approach to the problem, we want to employ a lightweight acquisition procedure with conventional photographic equipment.

3.4 Empirical Study

To study the effects of translucency on the accuracy of photometric stereo, we simulate subsurface light transport in a simplified setting, using a fully simulated target object (surface), camera, and light sources. This allows us to carefully control all of the relevant parameters and study the influence of each of the translucency parameters separately. Our goal is to vary these parameters, as well as the index of refraction of the test material, and analyze the output of photometric stereo to gain intuition about the effect of translucency on the quality of the results. To begin, we consider a simulation of a homogeneous, optically dense, translucent material as our target surface. We then progress to a physical setup.

Setup

In our simulation, we consider a homogeneous, optically dense, translucent material, and model the 8D BSSRDF [40] over incident position x_i , outgoing position x_o , incident direction ω_i and outgoing direction ω_o as the sum of a single scattering and a multiple scattering

term, as in Eq. 2.8:

$$S(x_i, \omega_i; x_o, \omega_o) = S^1(x_i, \omega_i; x_o, \omega_o) + S^d(x_i, \omega_i; x_o, \omega_o).$$

In our simulation of multiple scattering effects, we use the dipole-diffusion approximation of Jensen et al. [29] and for single scattering, we use the Hanrahan and Krueger model [22]. We ignore surface reflectance and assume directional (i.e., distant lighting). Furthermore, we only consider subsurface light transport and ignore interreflections.

The simulation scene consists of an orthographic camera looking down (along the Z axis) onto a planar homogeneous sample of $10cm^2$. The sample only exhibits sinusoidal surface depth variation (with a wavelength of $1cm$ and an amplitude of $\frac{\pi}{2}cm$) along the X axis, while remaining constant along the Y axis, as shown in Fig. 3.4. The surface sample is illuminated by a variable number of light sources equally distributed in a 40° cone around the view direction, ensuring that foreshortening is non-zero (i.e., $(n_{x_i} \cdot \omega_i) \geq 0$) for any surface point x_i and "directional" lighting direction ω_i . Unless noted, we employ three light sources in our simulations.

For each lighting direction, the outgoing radiance is computed for every surface point x_o at a resolution of 500×500 (a pixel to mm ratio of 0.2), and fed into a least squares photometric stereo algorithm. For each estimated photometric surface normal \hat{n}_{x_o} , the error with the ground truth normal n_{x_o} is computed as the angle between the estimated and ground truth normal expressed in radians: $|\arccos(\hat{n}_{x_o} \cdot n_{x_o})|$.

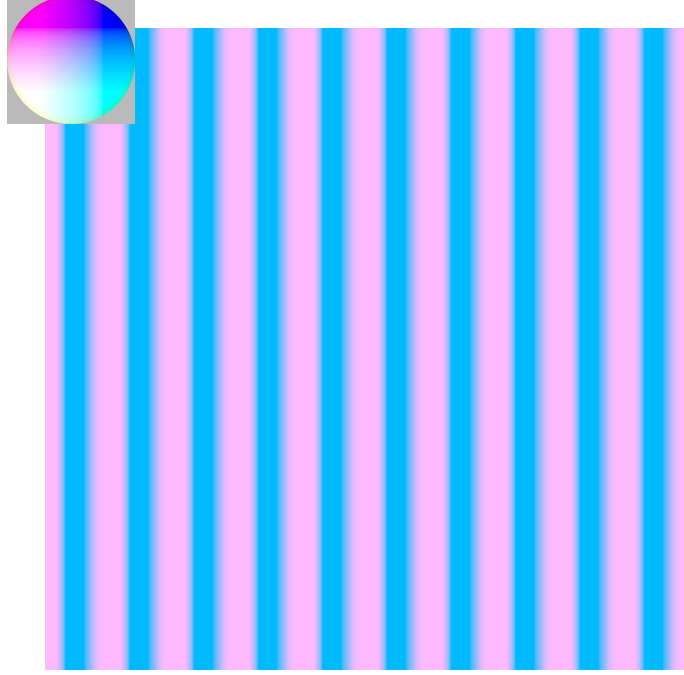


Figure 3.4: The ground truth normal map employed in our simulations. The sample size is $10cm^2$, and the amplitude of the sinusoidal normal variation is $\frac{\pi}{2}cm$. The inset shows the false-color coding of the normals.

Multiple Scattering

For our first experiment we only consider multiple scattering, and set $\eta = 1.0$ (i.e., $F_t = 1$), and $g = 0$. In this case, the outgoing radiance, $L(x_o, \omega_o)$, from Eq. 2.10 becomes:

$$\begin{aligned} L(x_o, \omega_o) &= \frac{1}{\pi} \int_A F_t((\omega_o \cdot n_{x_o}), \eta) R_d(||x_i - x_o||) F_t((\omega_i \cdot n_{x_i}), \eta) L_i(x_i, \omega_i) (\omega_i \cdot n_{x_i}) dx_i, \\ &= \frac{1}{\pi} \int_A R_d(||x_i - x_o||) (\omega_i \cdot n_{x_i}) dx_i. \end{aligned} \quad (3.3)$$

We only consider one incident light direction, ω_i , and the diffusion approximation, R_d , serves as the multiple scattering component of this simplified version of the BSSRDF. Here, we see that because the incident light direction ω_i is independent of the result of subsurface diffusion, that ω_i can be drawn outside of the integral:

$$= \frac{1}{\pi} (\omega_i \cdot \int_A R_d(||x_i - x_o||) n_{x_i} dx_i). \quad (3.4)$$

However, we can also consider this dot product in its full form, in which each component is multiplied before being summed:

$$\omega_{ix} \int_A n_{x_{ix}} R_d dx_{ix} + \omega_{iy} \int_A n_{x_{iy}} R_d dx_{iy} + \omega_{iz} \int_A n_{x_{iz}} R_d dx_{iz},$$

which amounts to taking the inner product of ω_i and a surface normal that is being modulated by the diffusion function, this altered normal designated as, \hat{n}_{x_o} :

$$= \frac{\gamma_{x_o}}{\pi} (\hat{n}_{x_o} \cdot \omega_i). \quad (3.5)$$

in which γ_{x_o} is a spatially varying scale factor that represents variations in the albedo map, and \hat{n}_{x_o} is the normalized blurred surface normal that is the result of the sum of the surface normals around x_o weighted by the diffuse reflectance R_d . The spatially varying scale factor depends on the incident Fresnel transmittance. Given that Fresnel transmittance depends upon the angle between the incident light direction, ω_i , and the surface normal at that point, the frequency of this scale factor is directly dependent on the spatial frequency and complexity of the object's surface.

Despite a varying albedo of γ_{x_o} , Equation (3.5) is roughly the Lambertian reflectance model, the blurred normal \hat{n}_{x_o} standing in for the true surface normal. An alternative interpretation is that the blurred normal is proportional to the convolution of the normal field with the diffuse reflectance: $\hat{n}_{x_o} \sim (n * R_d)_{x_o}$. The eventual result of computing photometric stereo on this surface will be the blurred surface normal \hat{n}_{x_o} .

From this analysis it follows that the accuracy of photometric stereo on a translucent material (only exhibiting multiple scattering and with an index of refraction of 1.0), depends on the shape of the diffuse reflectance R_d . If R_d is a delta function (and thus no subsurface scattering occurs), then the blurred normal \hat{n} will exactly match the ground truth normal n . To better understand the impact of the shape of the diffuse reflectance R_d , we plot (Fig. 3.5) the average error on the setup described above for a dense sam-

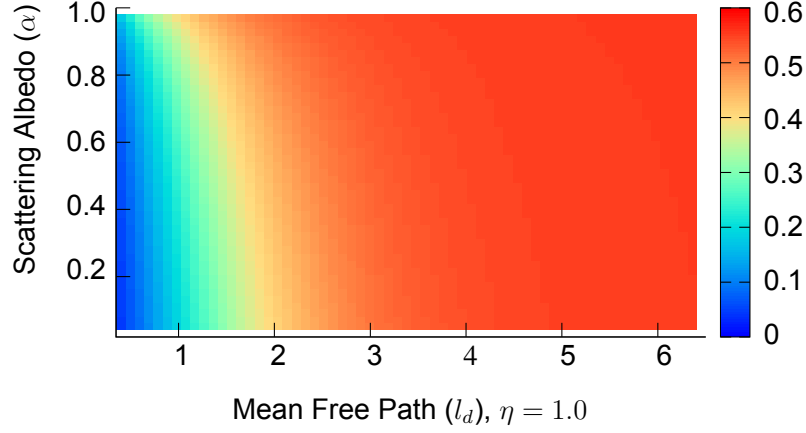


Figure 3.5: The average angular error plot for photometric normals computed from observations under three directional light sources, and for multiple scattering only, without taking Fresnel transmittance into account (i.e., $\eta = 1.0$) for scattering albedo $\alpha \in [0.1, 1.0]$ and mean free path $l_d \in [0.35, 6.5]$.

pling of scattering albedo α (vertical axis ranging from 0.1 to 1.0) and mean free path l_d (horizontal axis ranging from 0.35 to 6.5)

From Fig. 3.5 it can be seen that the average error increases with increasing l_d -- increasing mean free path implies a more translucent material. Indeed, at the extreme right, the extent of the diffuse reflectance profile significantly exceeds the wavelength of the sinusoid, and all normal variation is essentially blurred away. This is illustrated in Fig. 3.6 where we repeat a single line (horizontal) from the recovered normal map for a fixed $\alpha = 0.8$ and increasing l_d (vertical). Note that changing the wavelength of the sinusoidal surface variation, is equivalent to scaling mean free path inversely by the same scale factor [13]. Thus, changing the relative size of the geometric features results in a similar average error plot but scaled along the Y-axis.

Effect of Index of Refraction

The previous analysis employs an index of refraction of 1.0 which is not very realistic. If we allow the index of refraction to take on other values than 1 (i.e., $F_t \neq 1$), then we can make two observations. First, the exitant Fresnel transmittance term is independent of x_i

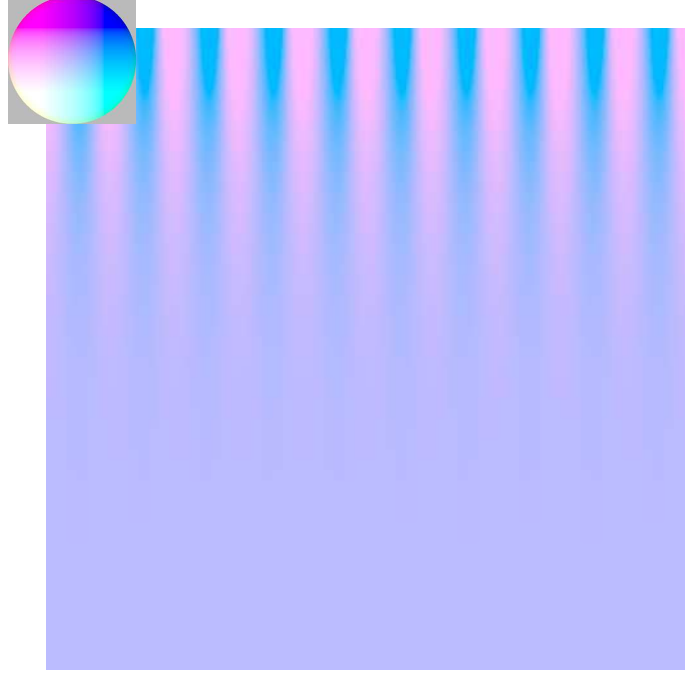


Figure 3.6: The impact of varying mean free path (vertical axis) on a slice from the normal map. As mean free path increases, the features in the normal map gradually become blurred out.

and thus does not impact the integral over the irradiance. Second, for plausible indices of refraction, F_t remains fairly constant over a large portion of its domain, varying only significantly towards grazing angle. However, towards grazing angle the foreshortening goes to zero, limiting the impact of the drop in Fresnel transmittance. Therefore, we can approximate $F_t((\omega_i \cdot n_{x_i}), \eta)(n_{x_i} \cdot \omega_i)$ by $F_{t0} \times (n_{x_i} \cdot \omega_i)$, where the scalar F_{t0} is the transmittance at normal incidence (Fig. 3.7). Thus, we can arrive at Equation (3.5) more generally as follows:

$$\begin{aligned}
 L(x_o, \omega_o) &= \frac{1}{\pi} \int_A F_t((\omega_o \cdot n_{x_o}), \eta) R_d(||x_i - x_o||) \\
 &\quad F_t((\omega_i \cdot n_{x_i}), \eta)(\omega_i \cdot n_{x_i}) dx_i, \\
 &\approx \frac{F_{t0} F_t((\omega_o \cdot n_{x_o}), \eta)}{\pi} \\
 &\quad (\omega_i \cdot \int_A R_d(||x_i - x_o||) n_{x_i} dx_i), \\
 &= \frac{\gamma_{x_o}}{\pi} (\hat{n}_{x_o} \cdot \omega_i),
 \end{aligned} \tag{3.6}$$

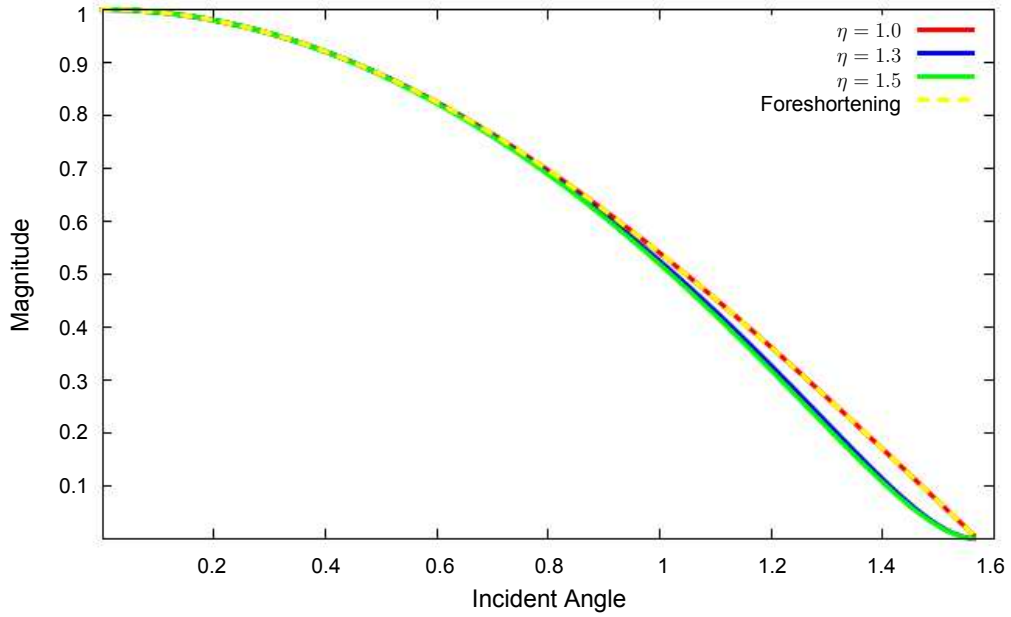


Figure 3.7: A comparison of $\frac{F_t(\omega_i, \eta) \max(0, \omega_i \cdot n_i)}{F_{t0}}$ for varying indices of refraction.

where the Fresnel transmittance terms are absorbed in the scale factor γ_{x_o} , yielding a similar expression as before. In Fig. 3.7 the diffuse reflectance R_d changes only slightly in shape as index of refraction changes. This justifies an approximation of $F_t((\omega_i \cdot n_{x_i}), \eta)(n_{x_i} \cdot \omega_i)$ by Fresnel transmission at normal incidence.

Fig. 3.8 shows the average error for indices of refraction of 1.1, 1.3 and 1.5. As predicted, the difference with the average error plot (with index of refraction of 1.0) shown in Fig. 3.5 is minimal.

Single Scattering

As we saw in Equation (2.13), observed radiance from a translucent material is a linear combination of the contributions from single scattering and multiple scattering. Because photometric stereo is also a linear process, each resulting normal that it computes is also a linear combination - of the blurred multiple scattering normal \hat{n}^d , and the single scattering

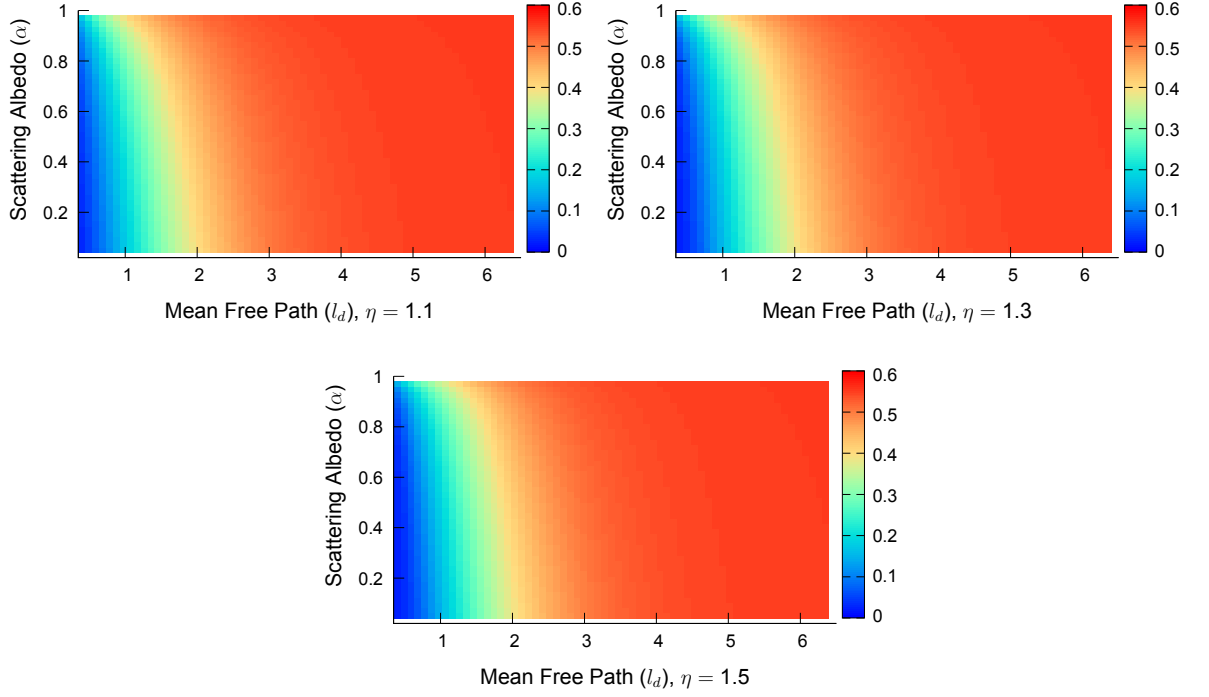


Figure 3.8: The average angular error plot for photometric normals computed from observations under three directional light sources, and for multiple scattering only, with varying index of refraction $\eta \in \{1.1, 1.3, 1.5\}$, for scattering albedo $\alpha \in [0.1, 1.0]$ and mean free path $l_d \in [0.35, 6.5]$.

normal \hat{n}^1 :

$$\hat{n}_{x_o} = \frac{\gamma_1 \hat{n}_{x_o}^1 + \gamma_d \hat{n}_{x_o}^d}{|\gamma_1 \hat{n}_{x_o}^1 + \gamma_d \hat{n}_{x_o}^d|}. \quad (3.7)$$

The relative contribution of single scattering to the resulting estimated photometric normal depends on the normalization constants γ_d and γ_1 , which in turn depend on the mean cosine g . Fig. 3.9 shows error plots for $g = -0.5, 0.0, +0.5$. We observe that, while the accuracy improves for all cases, the impact of backscattering (i.e., $g < 0$) is stronger than of isotropic scattering ($g = 0$), which in turn is stronger than forward scattering. However, for $|g| \rightarrow 1$, the reflectance behavior is significantly non-Lambertian, at which point the presence of single scattering negatively impacts the accuracy of the estimated normals.

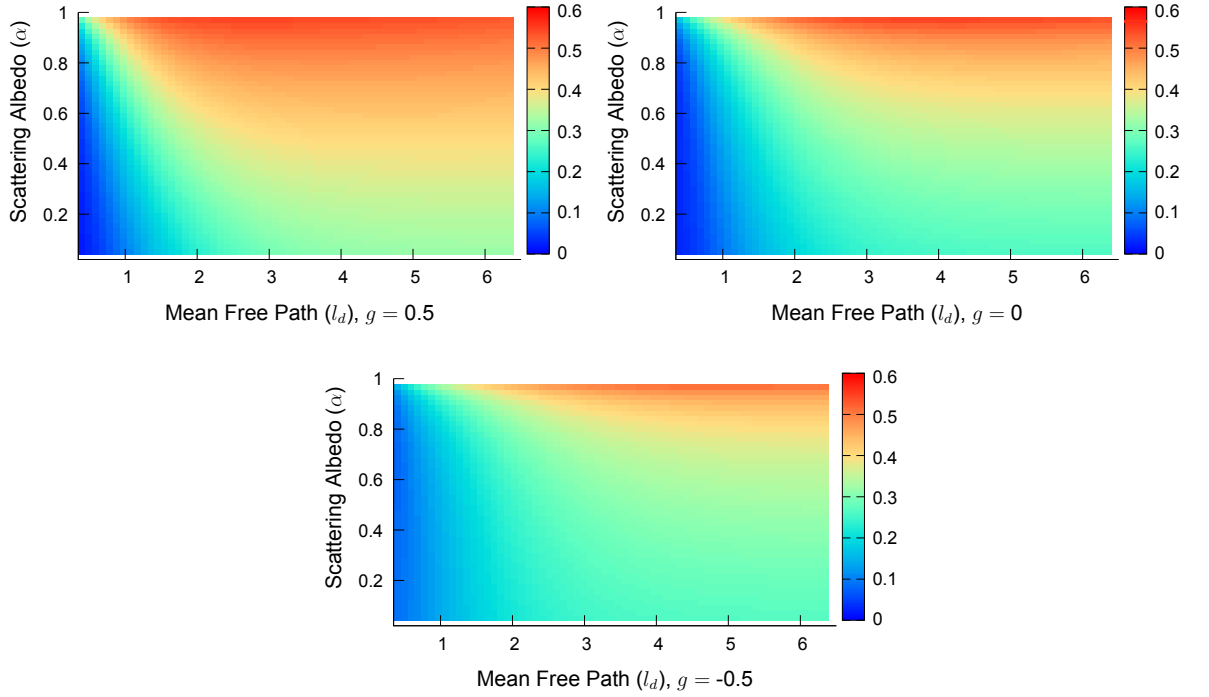


Figure 3.9: The average angular error plot for photometric normals computed from observations under three directional light sources, and for multiple scattering and single scattering (i.e., $\eta = 1.3$) with the mean cosine $g \in \{-0.5, 0.0, +0.5\}$, for scattering albedo $\alpha \in [0.1, 1.0]$ and mean free path $l_d \in [0.35, 6.5]$.

Lighting Directions

As a final, simulated experiment, we increased the number of light source from three to four, and solve for the photometric normal in a least squares sense. Using more than three light sources helps in improving the photometric normal estimate for regular, diffuse surfaces. Fig. 3.10 shows the average error plot for multiple scattering ($\eta = 1.3$). Due to the diffusion of exitant radiance, increasing the number of light source does not provide additional information, and the obtained photometric normals are identical. From this it can be concluded that increasing the number of light source directions, will not yield a significant improvement in accuracy.

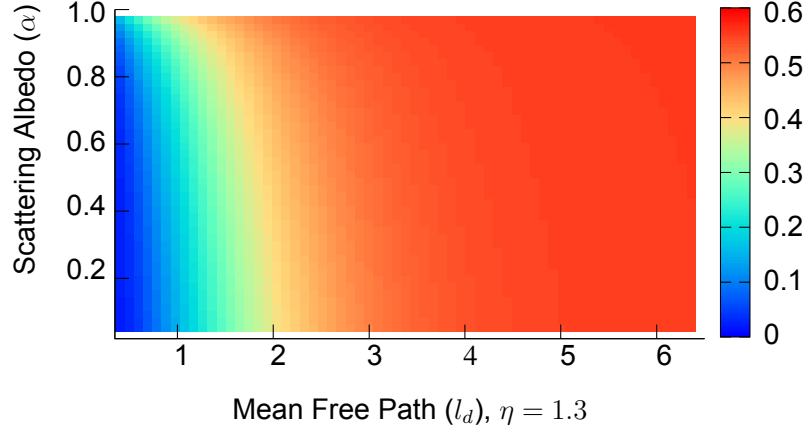


Figure 3.10: The average angular error plot for photometric normals computed from observations under four directional light sources, and for multiple scattering only, with $\eta = 1.3$, scattering albedo $\alpha \in [0.1, 1.0]$ and mean free path $l_d \in [0.35, 6.5]$.

Physical Validation

We show the validity of our analysis by capturing the photometric normals of a translucent soap sample. For the capture setup, we position 3 (or more) Quantum flash light sources at different positions that will illuminate the target object. Again, in practice, the target object is sufficiently smaller than the cone of illumination such that the flashes take on a pseudo-directional role. The camera should be placed at a position that maximizes the vantage of the illuminated portion of the object in each photograph. Three or more photographs are taken from this view direction, each illuminated by a different flash direction. This essentially provides us with three different samples of the outgoing radiance at each point, to use as our input L matrix. As long as the light source directions in D are also known, we can solve for N . Light source directions can be calibrated for using a Spectralon or specular sphere.

We estimate both the normals from multiple scattering only, and from the full subsurface scattering light transport (i.e., single scattering and multiple scattering). Our setup consists of a DSLR camera located approximately 1.5m away from the subject, and four flash light sources placed around the camera aimed at the sample. We place a linear polarizer in front of the camera, and to the light sources. We tune the linear polarizers on

the light sources such that specular reflections from a dielectric ball are canceled out (i.e., cross polarized). We calibrate the light directions and intensities of the individual flash lights using a Spectralon sphere. Next, we capture two pairs of four photographs, one pair cross polarized I_i^0 , and one pair I_i^{90} where we rotate the linear polarizer on the camera by 90 degrees. The images I_i^0 will only display (half of) multiple scattered light, and I_i^{90} contains all reflected components: (half of) multiple scattering, (full) single scattering, and is potentially polluted by specular surface reflectance. The sum of both $I_i = I_i^0 + I_i^{90}$ is equivalent to a photograph without a polarization filter in front of the camera.

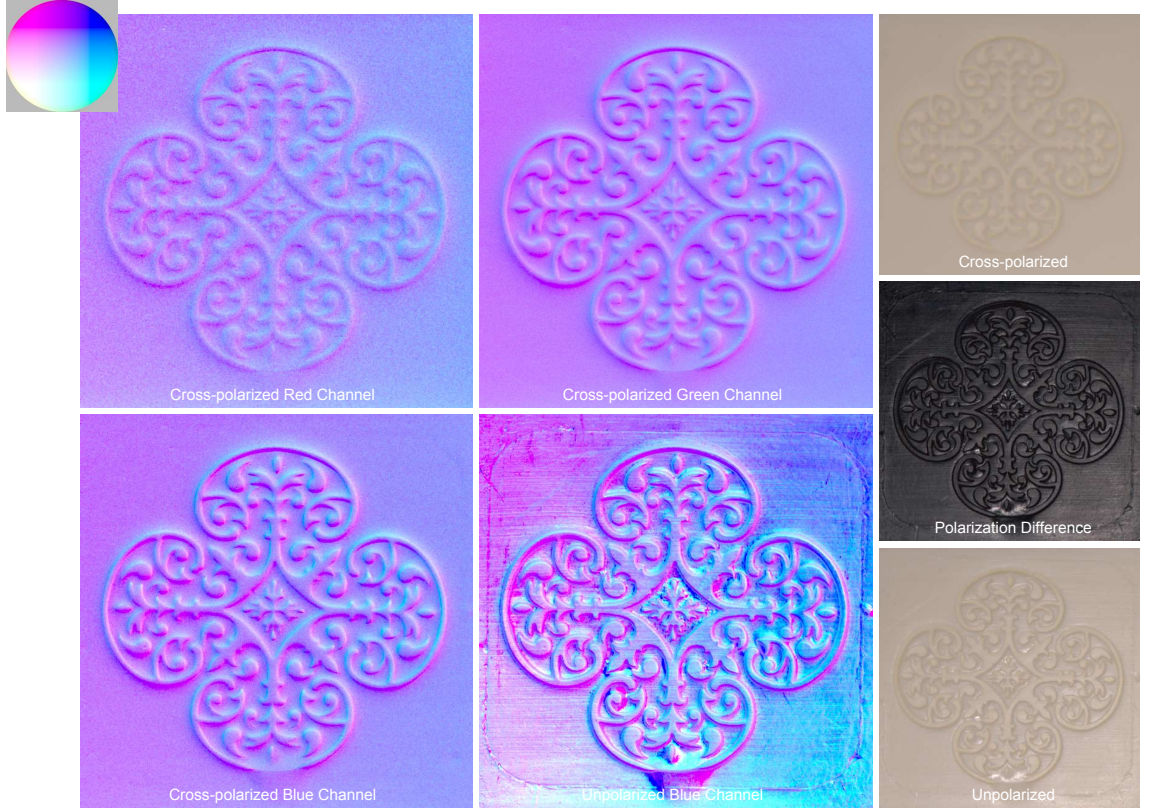


Figure 3.11: Left: Photometric normals estimated from a translucent soap sample. Note how multiple scattering blurs out most surface details compared to the multiple+single scattering photometric normal map. Further observe the effect of the wavelength dependent diffuse reflectance R_d on the sharpness of the photometric normals. **Right-top:** a cross-polarized captured image, exhibiting only multiple subsurface scattering, used to compute the multiple scattering photometric normals. **Right-middle:** polarization difference image showing the specular surface reflectance and single scattering removed by cross polarization. **Right-bottom:** unpolarized photograph of the translucent soap, showing both reflectance due to multiple as well as single scattering.

Fig. 3.11 shows (on the right from top to bottom) $2I_i^0$, $I_i - 2I_i^0$, and I_i for a single lighting direction. The difference image shows the amount of single scattering that was canceled out in I_i^0 . Note, that this difference also clearly contains some specular "pollution", which will affect the photometric results. Fig. 3.11 (right) shows the resulting photometric normals computed from I_i^0 (computed separately for the red, green and blue color channels) and the photometric surface normals computed from the blue color channel of I_i .

As predicted by our analysis, it can be clearly seen that the photometric normals computed from only multiple scattering exhibits very little surface detail. Since mean free path and scattering albedo are wavelength dependent, the "blur" kernel R_d differs. Consequently, the photometric surface normals for the different color channels differ slightly, resulting in blurrier normals for the red color channel (longer wavelength), and the sharpest normals for blue (shorter wavelength). This illustrates, that indeed as predicted, an increase in mean free path yields more blurred surface normals, and thus less surface details. While the photometric normals computed from I_i are biased due to specular surface reflection, it can be seen how much surface detail is lost by only considering multiple scattering.

Our input and assumptions for both the simulation and physical experiment were relatively idealistic. It would be interesting to replicate this experiment but while also including interreflections, not cross-polarizing to remove specularity, and finally validating with a full particle simulation. The drawbacks suffered by using the photometric stereo method on translucent objects are also pertinent to shape-from-shading methods, so this type of rigorous study has valuable application as-is and as a model for future investigations.

3.5 Conclusion

The benefit of this rigorous study is that we have identified which are the key contributing parameters to error on estimation of surface normals for translucent objects when using photometric stereo. Neither index of refraction nor scattering albedo have a large impact

on the severity of the error. Rather, it is the relative size of the mean free path versus geometrical feature size that strongly dictates the accuracy of results. We have validated this in simulation and with a physical sample and setup.

Essentially, the estimation of the surface normals of a translucent object using photometric stereo results in a blurred version of what the result would have been, had the object been Lambertian in appearance. This finding also establishes the remainder of our work in this dissertation, as we explore the effect and control of surface normals on appearance of objects comprised of many kind of materials.

Chapter 4

Normal Estimation Refinement for Translucent Materials

The previous empirical study highlights a key fact: increasing translucency sufficiently disassociates reflected radiance from incident irradiance so as to render the photometric stereo method for computing surface normals (and potentially shape-from-shading techniques) inaccurate. The simple fundamentals of the method and its usability remain attractive, however. Additionally, the wavelength of incident illumination has as an additional, significant effect on the quality of estimate of the surface normals. These contributing factors lead us to wonder what information about this disassociation can be retrieved from the original image to tailor a surface normal estimation and correct for any of its inaccuracies.

Therefore, as a continuation of our findings, we have developed a procedure for taking multispectral (red, green, blue) photometric surface normals calculated for a translucent object and inferring both the ground truth normals and the scattering and absorption (reflectance) coefficients. This idea developed from the observation that the photometric normals estimates tended towards greater accuracy with shorter wavelengths of light. This suggests that, given the proper constraints, the solution can be pushed towards the limit case - ground truth normals - while incidentally estimating the reflectance coefficients that led to each successive estimate.

4.1 Prior Work

There has been significant work on estimating the shape of translucent objects, as we explored earlier in the empirical study. There has also been extensive work on estimating the subsurface scattering properties of translucent objects. Despite this, we believe that the small acquisition overhead that our method would require makes our approach more lightweight.

A significant amount of previous research has relied on more explicit methods for acquisition of the scattering and absorption coefficients that dictate subsurface scattering behavior. For example, Jensen et al. [29], Goesele et al. [19] and Weyrich et al. [46] use lasers and a custom contact-measurement device, respectively, to discretely sample the subsurface diffusion profile of translucent objects. In a similar fashion, Ghosh et al. [16] and Peers et al. [41] employ high frequency illumination patterns to sample the subsurface diffusion at various points on the surface of objects. Any of these approaches can be hindered by surface mesogeometry that disrupts the reading of the diffusion profile. Rather than work around geometric features, our approach incorporates them in the refinement towards the final estimation of reflectance parameters in the optimization. Our approach also does not require high frequency illumination, only requiring the original, directional lighting already used in the photometric stereo process.

Not all previous research has required high-frequency lighting. Donner et al. [14] indirectly estimate the concentration of chromophores in skin from multispectral observations, but the approach is limited to skin. Zhu et al. [50] relate surface curvature to dipole parameters, but require a complex gantry for lighting and photography, which is more than the setup or data that we require and acquire using photometric stereo.

In our solution, we prioritize minimization of input to the system and prior knowledge about the material of the object surface at hand. We jointly refine both the initial, inaccurate estimation of surface normal values for a translucent object and the parameters that dictate this particular material's degree of translucency, namely α' and l_d .

4.2 Background

In the discussion of the BSSRDF in Chapter 2, we present the model for multiple scattering, Eq. 2.9. It incorporates the Fresnel transmission terms (incident and exitant) and the function for diffuse reflectance of subsurface light transport. These terms are modulated by the energy-conserving constant, $\frac{1}{\pi}$. This equation can be used in describing outgoing radiance but 2.9 is not, on its own, a model for calculating outgoing radiance.

By incorporating L , the incident irradiance term, and foreshortening (the dot-product between the incident lighting direction ω_i and the surface normal at that point, n_{x_i} , we can then integrate over all incident lighting directions and area on the surface, A to arrive at a formal expression of outgoing radiance emanating from a translucent object in Eq. 4.1. This is described in more detail in Jensen et al. [29].

$$L(x_o, \omega_o) = \frac{1}{\pi} \int_A F_t((\omega_i \cdot n_{x_i}), \eta) R_d(||x_i - x_o||) F_t((\omega_o \cdot n_{x_o}), \eta) L(\omega_i) (\omega_i \cdot n_{x_i}) dx_i. \quad (4.1)$$

The diffusion approximation function, R_d , can be substituted with any appropriate model. In reference to our empirical study, the dipole approximation from Jensen et al. [29] is an appropriate choice for homogeneous applications. However, a more recent formulation of a BSSRDF diffusion function, based on the dipole model, is the photon beam diffusion model by Habel et al. [21], which is more robust to non-planar surfaces and oblique illumination angles. Recall that a good diffusion function will take into account α and l_d , the main translucency parameters. Again, the value of α is tied to the magnitude of the peak of the BSSRDF kernel, and the magnitude of l_d is approximately proportional to the width of the kernel. Therefore, appearance of observed radiance, the image observed by a camera or our eyes is highly dependent on the settings of these parameters.

Indeed, from our previous work, we have seen that the BSSRDF can also be considered a "blur" on what the photometric stereo result would be for the same surface

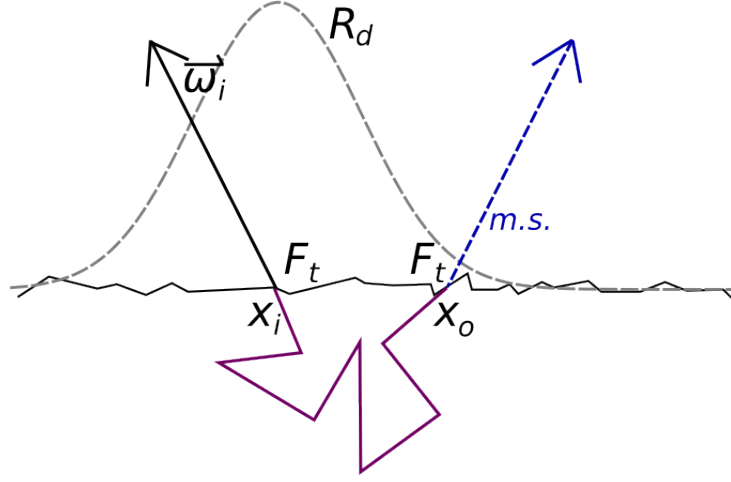


Figure 4.1: The predominant signal that is convolved by the blurring effect of subsurface scattering, is incident irradiance and its interaction with the surface normal at the point of incidence, x_i . Thus, outgoing Fresnel transmission at the point x_o can be considered independently of the blurring operation.

orientation but with Lambertian reflectance. It is a blur, in fact, on incident irradiance. Thus, from Eq. 4.1, we can pull out the effect of outgoing Fresnel transmittance from this blurring, rewriting the equation (for incident lighting direction ω_i) as such :

$$L'_{\omega_i} = R_{d\omega_i} * I_{\omega_i} \quad (4.2)$$

with L' representing outgoing radiance divided by outgoing Fresnel transmittance, and I the product between the foreshortening factor and incident Fresnel transmittance. This is illustrated in Fig. 4.1, as one can see that the diffusion is a blurring centered around the point of incidence and not strongly tied to the point of exitance.

Recall, also, the formulation of the observed radiance for general multiple scattering. In Eq. 3.5, we have derived observed radiance for translucent materials in terms of a convolution of the ground truth normal with the diffusion approximation formulated as a kernel. If there were no impact of Fresnel transmission (i.e. $F_t = 1.0$), then essentially, each blurred normal, \hat{n} , is the result of the operation shown in Eq. 4.3, a convolution between the diffuse BSSRDF R_d and the ground truth normal, n :

$$\hat{n} \sim R_d * n. \quad (4.3)$$

Given this formulation, a deconvolution should retrieve the original, ground truth normal. Of course, any deconvolution is ill-posed and can never fully retrieve the original, unadulterated input. Also, there is generally a non-trivial contribution of Fresnel transmittance. Even an approximation of the ground truth signal, however, would be an improvement on the blur.

Hence, in this experiment, we perform a blind deconvolution on the set of questionable surface normals, to recover the ground truth. Moreover, as we progress through the blind deconvolution, which we formulate as an iterative, preconditioned conjugate gradient method, we can not only acquire a better estimate of the surface normals but also simultaneously refine the translucency parameters and refine them, determining which values give us the "blurred" normals with which we began. However, we choose to recover not α , but $\alpha' = \frac{\sigma'_s}{\sigma_s + \sigma_a}$ because $\sigma'_s = \sigma_s(1 - g)$, thus giving us further control over the directionality of scattering in the refinement of the estimation. The process then becomes a joint optimization, simultaneously and alternately recovering the parameters of translucency and the ground truth normals.

Since we already use photometric normals as input, we do not have to perform a separate shape-estimation step like many other approaches. This is, in fact, the entirety of the set of geometric information that must be acquired for the entire joint optimization process. The RGB surface normals to refine, along with the observed radiance images, and initial estimates for the translucency parameters, are the input to the optimization. Recall also, from our previous study, that the results of photometric stereo on translucent objects are wavelength dependent. This means that we should always take care to exploit this progression of detail that is revealed with illumination by increasingly shorter wavelengths. Closely inspect Fig. 4.2 and notice the fine creases of the hand that become more visible as shorter wavelengths, towards ultraviolet, light are used. For this reason,

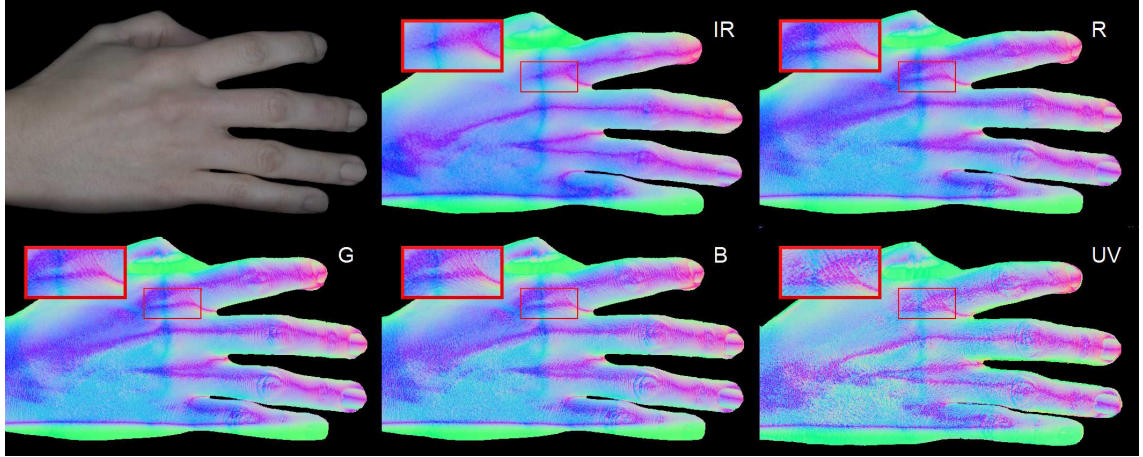


Figure 4.2: Results of photometric stereo computed from images of a hand illuminated in infrared, red, green, blue, and ultraviolet light.

we consider our algorithm in both per-channel and multi-channel variations, across the visible electromagnetic spectrum.

4.3 Project Overview

From the output of photometric stereo (normalized surface normals), we can initialize the joint optimization for acquiring both the estimated ground truth surface normals and the reflectance parameters for the particular material that comprises the object. The general procedure is to deblur the irradiance calculated from the input, estimate the reflectance parameters for computation of the dipole model for subsurface diffusion, re-estimate the surface normals, and compare regenerated irradiance images to the original, deblurred irradiance images in a least squares fashion. It is this comparison that propels the joint optimization towards further refined normals and reflectance parameters. The following section describes the process in more detail.

Algorithm

Overall, the procedure is a joint optimization, which begins with input of the originally estimated photometric normals for each wavelength (R,G, and B.) The following procedure forms the basis of the optimization, wherein the L2 norm between the observed radiance images and re-computed radiance images (incorporating the current translucency parameter estimates) is minimized.

As part of the input, we have several (at least three) observed radiance images. Given these images, L , the optimization searches for settings of the translucency parameters, α and l_d that produces a diffusion kernel that, when convolved with the product of a given estimated normal map and lighting directions D , results in the observed radiance. It also simultaneously produces an improved estimate of the ground truth surface normals. The optimization used is the Hooke and Jeeves [26] method, chosen because it is not necessary to calculate the derivative of the gradient of the system at any point; the "function" itself is nonlinear and the search space unconstrained. Thus, this pattern-matching optimization technique is a good option.

Estimate Irradiance Images The initial aim is to recover irradiance images from the original observed radiance images. Initially, outgoing Fresnel transmission is removed from the observed radiance images, L . Because R_d is an effective blur on the incident irradiance and foreshortening factor, it has no effect on outgoing Fresnel transmittance. In other words, Eq. 4.1 becomes:

$$L(x_o, \vec{\omega}_o) \approx \frac{F_t((\omega_o \cdot n_{x_o}), \eta)}{\pi} (\omega_i \cdot \int_A R_d(||x_i - x_o||) F_t((\omega_i \cdot n_{x_i}), \eta) (\omega_i \cdot n_{x_i}) dx_i), \quad (4.4)$$

so $F_t((\omega_o \cdot n_{x_o}), \eta)$ can be divided from each value in L . This is done in keeping with the fact that for L' , outgoing radiance divided by outgoing Fresnel transmission, $L' = R_d * I$, and we wish to recover the parameters that produce R_d .

Deblur Irradiance At this point, we have estimates for α and l_d . Next, the algorithm

progresses, using α and l_d to form R_d , from which L is deconvolved, or “deblurred.” In this experiment, we use the photon beam diffusion method of Habel et al. [21] as the BSSRDF model. The deconvolution is performed using the preconditioned conjugate gradient (PCG) method. This gives an estimate of the *deblurred* irradiance, I .

Estimate Surface Normals Here, a running approximation of the surface normals \hat{n} is computed. The algorithm computes \hat{n} through not only photometric stereo but also a non-linear optimization (again, Hooke and Jeeves [26]), so as to mitigate the ingrained effect of incident Fresnel transmission. Returned with the estimated normals is the normalization factor, ρ , the albedo.

Blur with Estimated Translucency Parameters Subsequently, a running estimate of the observed radiance, L_{est} is computed from a re-blurring of \hat{n} with a kernel built with the current estimates for α and l_d , then by multiplying by outgoing Fresnel transmission, and finally taking the dot-product with the lighting directions in D . Consequently, the algorithm can compute the root mean square (RMS) error, $\|L - L_{est}\|_2$. This error is the overall metric that determines the fitness of the currently-estimated translucency parameters (which also implicates the value of the currently-estimated ground-truth normals.) The process repeats until the solution converges.

There are two driving factors in the above, joint optimization, which is also outlined in Fig. 4.3, a flow chart of the algorithm. One factor consists of the differences in irradiance estimates that naturally fall out of having estimated irradiance from constantly-changing reflectance parameters σ_a and σ_s , per light source. The other key contributor is the fluctuation of ρ throughout the optimization, which, as it achieves values closer to 1, would suggest an increasingly “Lambertian-like” estimated irradiance, and thus, an approximate ground truth estimate for the surface normals. Interestingly, the magnitude of this normalization factor is proportional to the level of accuracy of the current estimate of the translucency parameters themselves. To verify the accuracy of the current estimate in a way that is agnostic of noise, however, we compare the computed radiance images from the lighting directions and the current parameters to the observed radiance images.

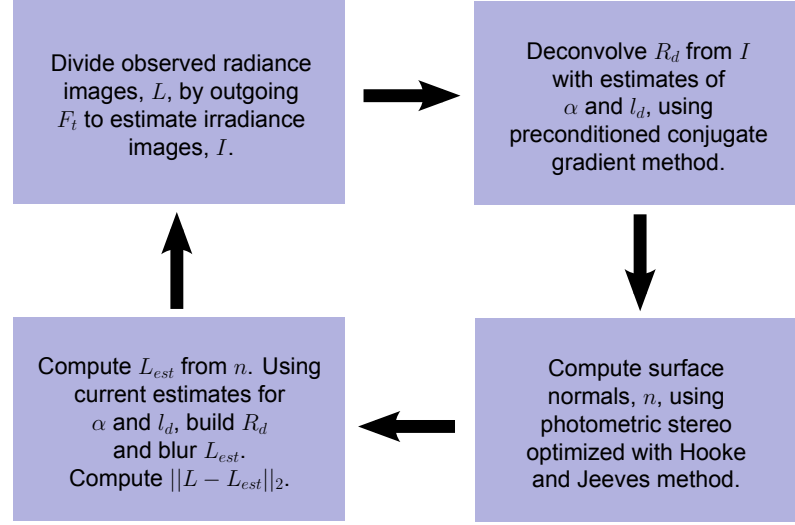


Figure 4.3: A flow chart of the ground truth surface normal and translucency parameter estimation algorithm. Overall, the error metric, $\|L - L_{est}\|_2$, is minimized via the Hooke and Jeeves method.

To further drive the solution towards a minimum, the optimization can incorporate the radiance calculations simultaneously, per color-channel, in the search space for a minimum. Light interaction with the material at hand differs, per color-channel, and not always in a deterministic way due to unforeseen material and chemical structure of the underlying material. Therefore, each channel will produce slightly different results for the estimated, recovered normals and thus the original translucency parameters.

Overall, the deblurring process requires the most time in this pipeline. Even with CUDA implementation for the GPU, and a target deblurring region of 80 x 80 pixels, the estimation takes 1-2 hours. For each color channel, c , the final result will take c times as long, as we obtain an estimate per color channel separately, then recombine them in a final, multi-channel joint optimization.

We also wish to see how well the estimation can work, given real ground truth data of an objects with the same surface normals, but each with either opaque or translucent characteristics. Thus, we built a capture system to verify results of the optimization.

Acquisition

It is non-trivial to find a pair of objects with exactly the same structure but comprised of different materials, one opaque and one translucent. So for validation purposes, we can sometimes build our own complementary pair. For instance, we use an opaque mold for the opaque object, and cast a translucent version out of soap, using the mold, for its translucent counterpart. This result is incorporated into our later results.

Calibration for real data requires a multi-pronged approach. As with photometric stereo before, we use a Spectralon sphere to calibrate for the light source directions, given the fact that we know the surface normals for a sphere. We must also calibrate for absolute radiance of the samples - in other words, because all light sources are not placed exactly equidistant with respect to each other and to the target object. Therefore, we must compensate for differences in light source power among all of the images, and for power fall-off within a given image. To do this, we divide each image of the target object by the respective image of a Spectralon plane.

Data acquisition for this project proceeds similarly to that of the empirical study. Throughout this pipeline, normals are estimated via photometric stereo. We try to ensure that the region of interest on the target object is globally planar to minimize error introduced by shadows, interreflections, and radiance falloff. Of course, we are interested in objects with microgeometric aberrations. Therefore, we place the plane of our target object perpendicular to the view direction of the camera. We then ensure that the camera is cross-polarized with respect to each flash and the target object to eliminate effects of specularities and single scattering. We then proceed with photometric stereo.

From here, we proceed with the traditional photometric stereo capture setup from the first study, in which we mount a DSLR camera (Nikon D700) among four, roughly equidistant light sources aimed at the target object. Then, radiance images are captured for each object, from which the surface normals can be calculated using the acquired lighting directions.

4.4 Results

Our results consist of running the algorithm on several captured translucent materials with varied surface mesostructure and comparing the results to known parameters for α and l_d as well as to the ground truth normals (if known.) We also have results of a simulation in which we apply translucent parameters to surface normals and try to retrieve what we know to be the ground truth.

Fig. 4.4 shows a sample output of the algorithm, an estimation of the ground truth normals captured from a sample of scored, pink soap. Because soap is a mold-able material, we were able to first capture the ground truth normals of a diffuse mold, then pour the molten soap on the mold, and calculated the result for the (inverted) translucent soap on the same geometry. We can see the per-channel original output of photometric stereo, followed by the per-channel refinement by the algorithm. One can see the improvement towards shorter wavelengths that penetrate the translucent material less, and thus scatter shorter distances below the surface. The result for the blue channel itself, Fig. 4.4(h) rivals that of the multi-channel optimization, Fig. 4.4(e). The last row shows the complementary result of the algorithm, the estimated BSSRDF scattering profiles from the estimates for α and l_d .

Noise, amplified by successive deconvolutions, becomes problematic in estimating the parameters and contributes to the error in estimation. One can easily see the amplified noise in the red channel estimation (f) of Fig. 4.5. Employing the multi-channel approach to estimation enables the algorithm to mitigate some of this noise because the signal can be regularized across all channels, resulting in a better estimate. Still, a degree of noise persists. Because it is usually difficult to make molds of desired translucent objects, most of our tests did not have the benefit of ground truth normals against which to compare results. There are, however, readily available measured parameters for l_d and α , acquired in a laboratory setting, against which we can compare results for other materials.

In Table 4.1, we see the estimated translucency parameters for a range of materials

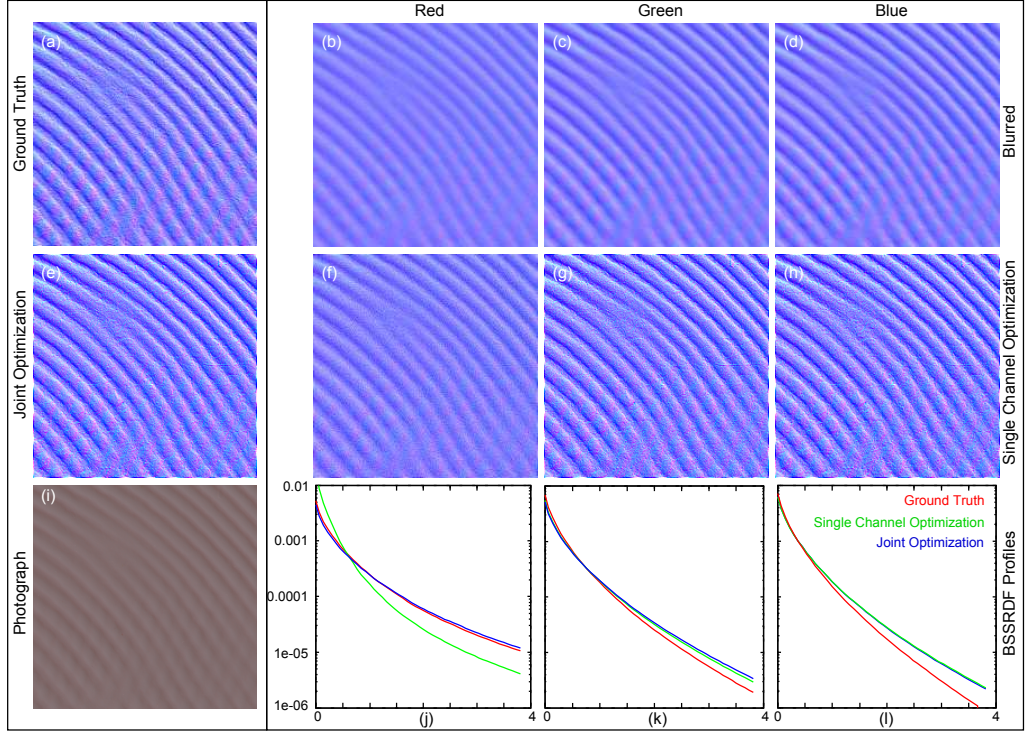


Figure 4.4: (a) Ground truth surface normals captured directly from the mold used to cast the normal variation on the pink soap material (i). (b-d) Naively applying photometric stereo directly on the observations yields blurred normals. (f-g) Result from our method computed on each channel separately. (e) Result from joint optimization on all color channels simultaneously. (j-l) Corresponding ground truth and recovered BSSRDF profiles.

for which we also estimated the ground truth surface normals. The mean free path, l_d , is more difficult to estimate than the scattering albedo, α . The amount of error incurred, however, has little effect on the overall scattering profile shape.

4.5 Discussion & Limitations

The overarching limitation of our method is that it is only applicable to globally planar surfaces. Significant curvature to the surface would result in a deformed scattering kernel, thus creating spatial variance in the effect of subsurface scattering on outgoing radiance, per surface normal. Our model is robust to slightly curved surfaces, however, and an interesting further trajectory would be to stress-test the system to determine the tolerance-

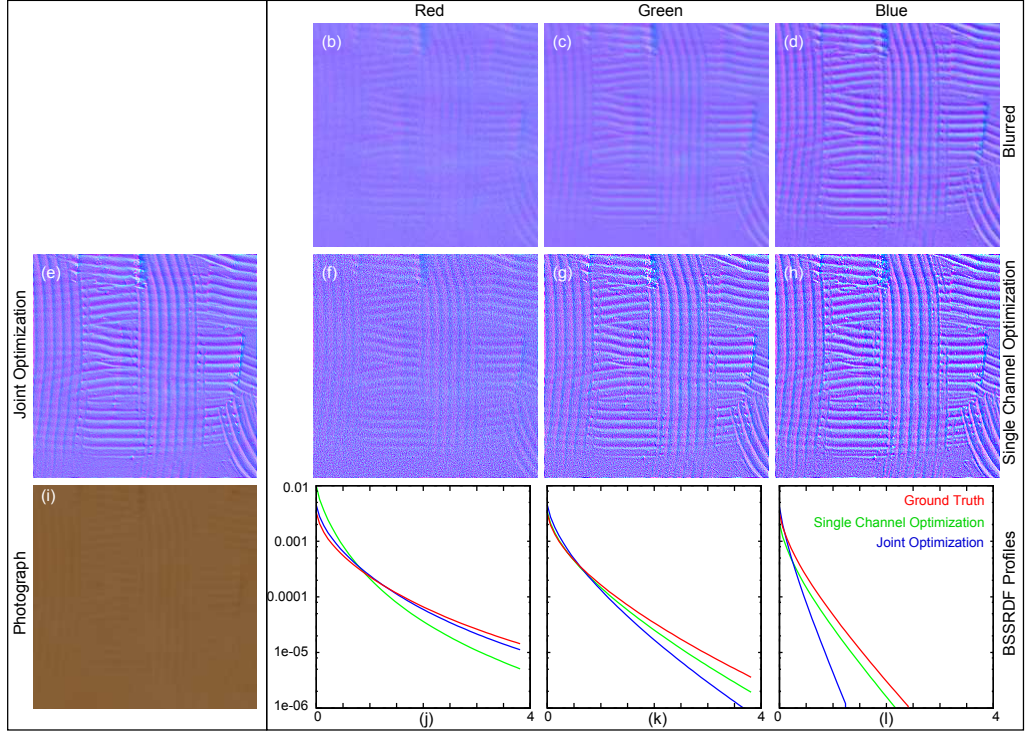


Figure 4.5: Result for Cheddar Cheese (i). For this example, no ground truth normals are available. **(b-d)** Naively applying photometric stereo directly on the observations yields blurred normals. **(f-g)** Result from our method computed on each channel separately. **(e)** Result from joint optimization on all color channels simultaneously. **(j-l)** Corresponding ground truth and recovered BSSRDF profiles.

level of the optimization in terms of surface curvature.

As in our first project, we use cross-polarized images to isolate multiple scattering in the observed radiance images. This is imperfect for translucent materials that have a more structural medium. This would be problematic for translucent crystalline materials such as a block of sugar, and in fact, the complex geometric network of the material would probably disrupt diffusion too much to use these types of materials as input.

The results of this system are promising, and we believe that we could incorporate a more advanced deconvolution algorithm in the future to improve further on these results. Ideally, we would be able to mitigate better the amplification of noise from successive deconvolutions. We look forward to broadening the capability of this optimization process.

Table 4.1: BSSRDF parameters estimated using the joint multi-channel deconvolution versus ground truth parameters.

Material	Parameter	R	G	B
Pink Soap	est. α	0.999	0.991	0.991
	g.t. α	0.999	0.992	0.987
	est. l_d	0.333	0.284	0.235
	g.t. l_d	0.288	0.221	0.207
White Soap	est. α	0.999	0.998	0.991
	g.t. α	0.999	0.999	0.998
	est. l_d	0.302	0.223	0.156
	g.t. l_d	0.309	0.219	0.179
Cheddar Cheese	est. α	0.999	0.968	0.790
	g.t. α	0.999	0.977	0.875
	est. l_d	0.329	0.289	0.168
	g.t. l_d	0.431	0.414	0.305
Potato	est. α	0.967	0.997	0.967
	g.t. α	0.999	0.996	0.956
	est. l_d	1.027	1.057	1.037
	g.t. l_d	1.029	0.947	1.025

4.6 Conclusion

All subsurface light transport data is inherently encoded in a photograph of a translucent object. Of course, this proliferation of light interactions is so complex, and so disruptive to the relationship between the incoming and outgoing irradiance and radiance positions that it is difficult to tease useful data from such a photograph. In this work, we have made progress in recognizing the effect of subsurface light transport on image-based surface normal calculations - effectively a blur on ground truth normals. By applying the typical inverse of a blurring operation, a deconvolution, we have both acquired a better estimate of the surface normals of a translucent object and a description of the blur itself. We hope that this algorithm can be further tested in the future for its robustness to curved surfaces and varying degrees of surface roughness. We look forward to fully describing the power of this method in the near future.

Chapter 5

Image-Based Microgeometry Manipulation

There is a great deal of potential for replicating three-dimensional effects through extracting reflectance and shape information from a single image of an object. In the case of estimating shape information, the results of photometric stereo and shape-from-shading (SfS) algorithms are highly dependent on the subject at hand. The material, the degree of translucency, and the surface mesostructure all contribute to the overall appearance of the object. Taken as this confluence of complicated, light-based interactions, we ask: how can we generalize the reflectance in a photograph, as-is, and use it to make image-based modifications to the surface mesostructure of an object? What are the challenging cases, and how can we mitigate these challenges for both a photo-realistic result and an enjoyable experience for the user? To explore these questions, we have constructed a system, a user-interactive interface for editing the surface mesostructure of an input object that automatically updates the reflectance in the original photograph.

5.1 Prior Work

Image-based shape editing is a growing research area. In one vein, the challenge of editing the shape of an object given limited information has been formulated in terms of two-dimensional textures. In the work of Fang and Hart [15] a texture on a surface is deformed when a user identifies source and target curves for the surface. The operation only occurs in image-space, however, and so does not serve to alter per-pixel surface orientation of the object in the image. Kautz et al. [31] have addressed shape-editing from the angle of the bidirectional texture function (BTF), a six-dimensional spatially-varying function for describing a texture from various view and illumination angles. However, the BTF-approach is generally too involved for photographic image-editing, in which surface mesogeometry ought to be plausible, but accuracy is not strictly necessary at the micro-geometric level. Others, such as Wu et al. [49] allow the user to perform edits at the fine, normal-level, but this project consists predominantly of refining only a normal estimation itself, considered to be poor. It does not do this in view of further appearance editing, and thus is itself too complex a process for our needs. In our approach, we would rather avoid the overhead of rigorously designing an explicit model such as a BTF and, instead, implicitly solve for the full hemisphere of values.

Another growing area for investigation are methods for editing reflectance using only image-based approaches, an attractive strategy that also avoids lengthy or impossible data acquisition in a laboratory environment. While Khan et al. [32] achieve promising results of edited materials from a single image, the edited reflectance is still limited to usage on the original geometry of the input material. Similarly, White and Forsyth [47] are limited to editing the reflectance of white or off-white objects in video frames. The artistic approach to applying a particular reflectance is to use a "lit sphere" approach in the vein of Sloan et al. [44], wherein the reflectance effects are encoded in a fully-described sphere for later application to drawn or rendered objects in the future. Continuing this idea, Zubiaga et al. [51] recreate the lit sphere for non-photorealistic objects for the transfer of

appearance. Sloan et al. and Zubiaga et al. do not account for shadowing as we do, and the latter work must have a full sphere of reflectance information from which to begin.

We have found particularly inspiring the work of Cabral et al. [7]. They present the idea of a reflected radiance map - a sampling of the hemisphere of possible exitant radiance responses to a particular lighting configuration, for a particular BRDF. They estimate the reflected radiance map for use in rendering the appearance of a novel object. They do not, however, account for real-world photographs as input or for complex BRDFs. To the best of our knowledge, no one has developed a system that will simultaneously estimate reflected radiance for a particular BRDF from real scenes and allow the editing of surface geometry.

The idea of appearance transfer, however, has been of increasing interest in graphics. An important milestone in appearance transfer is the work of Hertzmann et al. is "image analogies" [23]. Through their algorithm using paired reference images as a rule for appearance transfer, they achieve texture synthesis by example, but the resultant textures can be thought of as more like global, mesogeometry filters that achieve certain artistic effects. Each effect is taken from and applied to an image in a strictly two-dimensional sense; whereas we are interested in three-dimensional shape so that we may photo-realistically edit it and then transfer appearance. Similarly, Ramanarayan et al. [43] seek a visual equivalence metric in for identifying cases in which simpler illumination or geometry than that which was input may be used instead to achieve a desired effect. From the textural standpoint, Diamanti et al. [11] use exemplars to transfer appearance. This algorithm suffers in quality from cases of pattern-repetition, however. Our material-based approach maintains a smooth gradient regardless. We approach this project with appearance transfer in mind but require it to function in the context of real, naturally-lit objects and the materials from which they are composed.

Lastly, machine-learning/training-based techniques are currently used to solve similar problems in appearance transfer. The idea is that, given enough machine- or human-annotated input, the algorithm will "learn" relations between images. In the work of Laffont

et al. [33], outdoor scenes can appear to change time of day or climate. In Glondou et al. [17], fracture-patterns are learned and applied to arbitrary objects to show wear. With these techniques and others like them in the area of machine-learning, the pre-processing or offline overhead is usually steep. Keeping in mind that we want our users to be able to, on a whim, import an image for editing, significant pre-processing time will not do. Thus, we have weighed what we would consider to be a tolerable online workload against convenience.

5.2 Background

This project differs from both of the previous projects discussed in a fundamental way. Thus far, we have seen projects that hold measurement accuracy as the priority, both from empirical and practical standpoints. Given what we have learned from these studies about the strong tie between appearance and microgeometry, we are interested in creating a framework whereby a user can input a photograph of an object in a real-world environment and an estimate of its surface normals, make edits to the microgeometry of the object, and let the system make the corresponding change to the object's reflectance. The heart of this project is grounded in the fact that, in most cases, all of the information required for further editing of surface orientation is already incorporated into the photograph of the scene.

Our approach is based on the editing of reflected radiance maps. Highlighted in Cabral et al. [7], a reflected radiance map is considered to be the complement to a traditional, incident radiance map, in which the hemisphere of incident light in a scene is reconstructed. The reflected radiance map is the hemisphere of responses to this incident radiance for a particular material, for one possible orientation of the hemisphere of directions.

In other words, one can consider a reflected radiance map to be the convolution of the traditional, irradiance map with the BRDF of a material. To illustrate this, picture an object, such as the mug in Fig. 5.1, made of a homogeneous material that possesses a certain



Figure 5.1: Mug illuminated with distant light. Image courtesy: [8].

degree of geometric aberration on its surface, placed in a well-lit environment. One could sample the reflected radiance for the material that comprises that object, at each known surface orientation point. With only a subset of samples, it would be feasible to interpolate for unknown values of radiance and to be able to solve for the entire reflected radiance map. From here, an interested user could then execute image editing operations that alter the known geometry of the object's surface and accordingly update the radiance through a look-up system of the reflected radiance map. This accessibility to known reflectance, with incorporated illumination, has motivated the image editing tool that we have created.

This is not a simple problem, as real-world environments present numerous challenges to appearance editing. The problem quickly becomes non-trivial for realistic examples of both the environment (irradiance) map and the BRDF. In the style of Cabral et al. [7], we assume distant lighting in the scene so as to generalize the relationship between a particular value for the resultant radiance map with a particular normal direction anywhere it is identified. This makes the problem tractable but also heavily constrains the types of objects for which the approach is initially valid. Any target object in the scene that exhibits shadowing or interreflections either from itself or surrounding objects becomes challenging, as the underlying BRDF may, in fact, be homogeneous but be immediately unrecognizable as such in the presence of these phenomena.

Extracting information from a photograph requires careful consideration of the interactions between materials and illumination. Teasing apart the relative contributions of re-

flectance and illumination is a severely under-constrained problem. To understand what is at play in a photographed scene, we consider both reflectance, environment illumination, and their combined effect.

Irradiance Environment Maps

Each surface point of an object illuminated in a photograph incorporates incident irradiance information from all visible angles at that surface point. An irradiance environment map is essentially a comprehensive description of the illumination emanating from all angles, incident to a point on a surface. In a photograph, irradiance E can be calculated as:

$$E = \int_{\Omega} L(x_i, \omega_i)(\omega_i \cdot n_{x_i})d\omega_i, \quad (5.1)$$

where L is the incident lighting at point x_i from direction ω_i ; and n_{x_i} is the direction of the surface orientation at the point x_i . This product is integrated among every direction over the sphere of directions, Ω .

An environment map is usually captured by taking two photographs of a specular globe and composing the photos to create a 360-degree depiction of the irradiance incident at that point in the scene. Depending on the lighting distribution, this signal can range in frequencies, adding to the potential complexity of the observed reflectance in the scene. Fig. 5.2 is an example of a rather high-frequency irradiance environment map (or “light probe”) [9]. This environment map can be used as a distant illumination source, surrounding a scene from the simple to the complex.

Understanding the concept of an irradiance map is helpful in understanding what is seen in a typical photograph of an object - the reflectance of both the incoming illumination in all of its complexity, combined with the reflectance of the object material itself. It is a difficult problem in computer graphics to tease apart material reflectance and illumination. What happens when the object in the scene is adjusted, its structure altered or rotated?

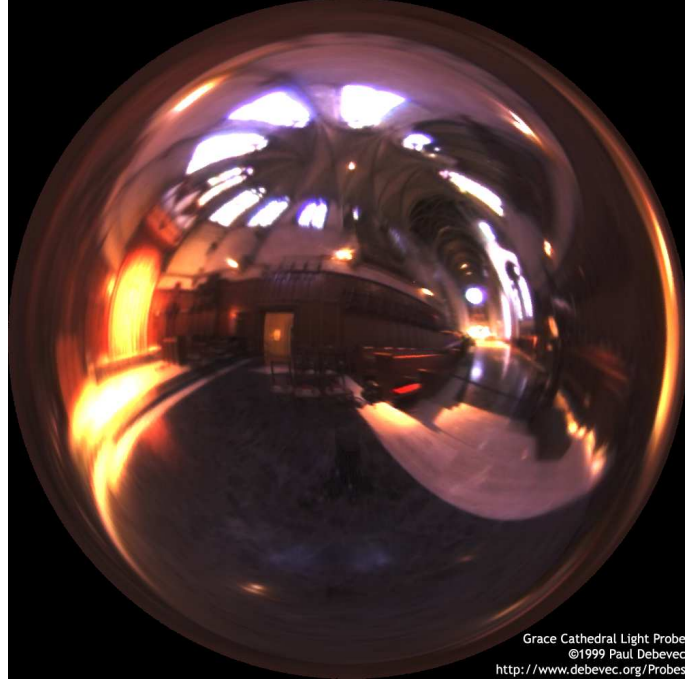


Figure 5.2: Example of a captured irradiance environment map [9].

At any given point, both its shading and its modulation by illumination will potentially be changed completely. For this reason, we are motivated to investigate the editing of surface normals in the context of a target object with illumination “baked in” to its material reflectance.

Reflected Radiance

As complex as incident irradiance illumination can be, the object itself reflect light in a complex way, depending on its BRDF and geometric properties. Our tool focuses on the editing of a target object in a photograph. Any edits to the object's surface geometry will affects it reflectance at those points, which in turn is a convolution between reflectance and the incident irradiance. Hence, observed radiance L_o at a point on the surface of an object is:

$$L_o = \alpha \int_{\Omega} f_r(\omega_i, \omega_o) L(x_i, \omega_i) (\omega_i \cdot n_{x_i}) d\omega_i, \quad (5.2)$$

where α is the surface albedo and $f_r(\omega_i, \omega_o)$ is the bidirectional reflectance distribution function (BRDF), which is the ratio of reflected radiance (in direction ω_o) to incident irradiance (in direction ω_i) at that point on the surface.

Comparing Eq. 5.2 with Eq. 5.1 again emphasizes that what results in a calculation of outgoing radiance is a convolution of the BRDF with the lighting factor. From one photograph alone, it is extremely difficult to automatically determine what reflectance values are due to surface reflectance and what result from incident lighting. If a full description of either of these values is provided, they can be separated. Typically, however, we do not have access to explicit descriptions of either BRDF or lighting. It is more convenient to be able to work with the reflectance convolved and as-is. Our system for editing reflected radiance works within this construct, that it is not worth the pre-processing effort of separating illumination, and still generates a photo-realistic result. Next, we discuss our solution for harnessing reflected radiance for image-based, surface mesostructure editing.

5.3 System Overview

The goal of this user-interactive system is to enable the user to make mesostructure edits to the surface of a target object in a photograph, as if the user is manipulating the texture of the surface in three-dimensions. For ease-of-use, we also prioritized limiting the input to the system. The operation is effectively that of a stamp, one that perturbs the underlying surface normals locally but maintains the global object shape. Depending on the "stamps" activated in the system, the user can make any number of edits to the surface mesostructure of the object.

Our main assumptions about the input to the system are twofold. First, we assume that there is a photograph of a target object to be edited, illuminated by approximately distant illumination, and that a mask has been applied to isolate the target object in the image. Practically speaking, the photograph is probably a scene of an object in a well-lit

room or outdoors in diffuse light. We will refer to this image as the "target image." The second assumption is that there is a way to obtain a decent approximation of the object's surface normals. It must be the case that either an image with pixel-to-pixel correspondence, encoding the surface normals, is included along with the target image, or that the illumination conditions of this target image permit the usage of the SfS technique in Barron et al. [2] to estimate the surface normals from the photograph. When photometric stereo data is not available as input, the system incorporates the SfS technique of Barron et al. to estimate surface normals. We chose this method for its robustness to heterogeneous materials. In either case, we encode each of the three-dimensional components of the surface normals as an RGB-value ($x \rightarrow R, y \rightarrow G, z \rightarrow B$) to facilitate extraction of this information. Given these two images, the system refines them for eventual extraction of reflected radiance information.

Image Pre-processing

Again, assuming that there is a per-pixel correspondence between the pixels of the target image and that of the surface normals, the system imports the images and processes them further. When working with photographs, haloing effects caused by spherical aberration can hallucinate nonzero pixel values for which there is no surface normal measurement. Anticipating this as a potential effect, the system first erodes the edges of the target object and surface normals using the OpenCV library "erode" function [6], and an example of this operation is shown in Fig. 5.3. From this, we can be sure that only valid pixels are considered for reuse in an image-based edit.

Binning

Following this pre-processing stage, the system then collects a series of information that culminates in the re-organization of the pixels into a latitude-longitude (lat-long), two-dimensional format, in which $0^\circ \leq \theta \leq 180^\circ$ and $0^\circ \leq \phi < 360^\circ$, and each of these



Figure 5.3: Left: Example of a rendered, glossy sphere input, which had been masked with the computed normals; however, hallucinated pixels remain around the rim. Right: Improved input, the edge of which has been eroded to remove the halo around the rim. Rendering: Mitsuba [28].

positions represents the surface normal value from the sphere of possible directions. For any given photograph of a target object, we will see roughly a hemisphere of normal values represented because the field of view of the camera will only be able to capture a hemisphere of three-dimensional directions, more or less. This, of course, depends on the angle of view of the camera lens. Each of these discretized ``bins" may represent one, many, or zero reflected radiance values depending on the shape of the object at hand. It is important to track all of the values attributed to each surface direction and, likewise, to all of the pixel locations on the target image that map to each lat-long value for later usage by the the algorithm for reflected radiance replacement later in the system.

Hole-filling

At this point in the system, we have all of the observed, reflected radiance collated by location. It is likely that not all of the possible directions on the hemisphere have been observed, so there will be ``holes" to take into account in case the editing operating shifts any normal values to these locations on the hemisphere. Because of this, we employ an interpolation scheme based on Delaunay triangulation.

For each missing value in the discretized, lat-long map of radiance values per normal position, the value is projected onto the unit sphere and located with respect to the nearest

three, known reflectance values. These values form the outer points of a triangle that is then subdivided into three sub-triangles that share the missing point. The interpolated value of this missing point, the centroid, c , is then calculated as the weighted sum of the values of the three, outer points. Finally, the centroid is projected onto the unit sphere, by the following metric, to determine to which hemisphere it should be projected:

1. Calculate the center of mass of all points in three-dimensional space, m .
2. Calculate the following two dot products, a and b , given the surface normal, n at each point p :

$$a = (n \cdot c)$$

$$b = (n \cdot m)$$

3. If a and b are both positive or both negative, do not change the sign of c .

Otherwise, $c = -c$.

This subdivision-projection scheme was chosen to approximate the spherical distribution of radiance incoming towards the target object. The center of mass is not necessarily on the unit sphere of points, hence this point needs to be reprojected to conform to the spherical distribution. This process is repeated based on a preset tolerance level for a side-length of a triangle. Once all sides are shorter than this length, the process is terminated. A visualization of this process is shown as a series of "inflated" convex hulls in Fig. 5.4.

The weight of each contribution is proportional to the ratio of the area of the sub-triangle that coincides with the missing point, to the area of the full triangle. Since it would be physically impossible to edit a normal to face the rear of the hemisphere of values and enable it to be visible, only the hemisphere of values is necessary. A before-and-after set of images depicting the reflected radiance map is shown in Fig. 5.5. From this point, the user can proceed to interact with the system, making edits with the application's tools.

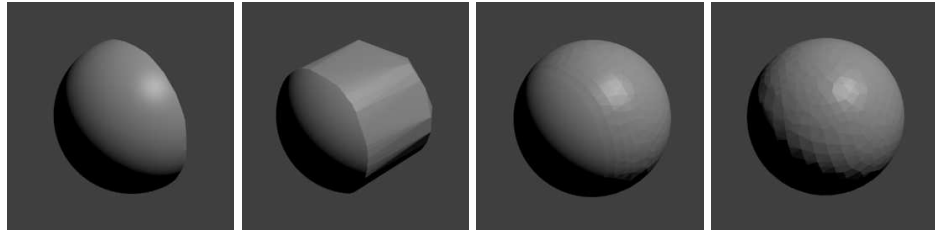


Figure 5.4: Progression of reflected radiance map "inflation" depicted as a convex hull generated from surface normal points input to the system. The inflation begins with the original input (left) and iterates, subdividing triangles and projecting points to the hull, to arrive at the final inflation (right.) Rendering: Blender [5].

Editing

As the user interacts with the system, he or she has the opportunity to perturb the mesostructure of the surface of the target object by applying functions that effectively stamp the surface of the object. The user can select a quadrilateral region of the surface which is then warped to mimic a three-dimensional application of a similar tool, using a homography. The homography warps the borders of the selection box according to the average normal direction of the underlying surface. Then, the user has a number of stamps to choose from, including: blur, randomized normals, sharpening, waves with alternating vertical pitches, squared bumps, and a dimple, a selection of which is shown in Fig. 5.6.

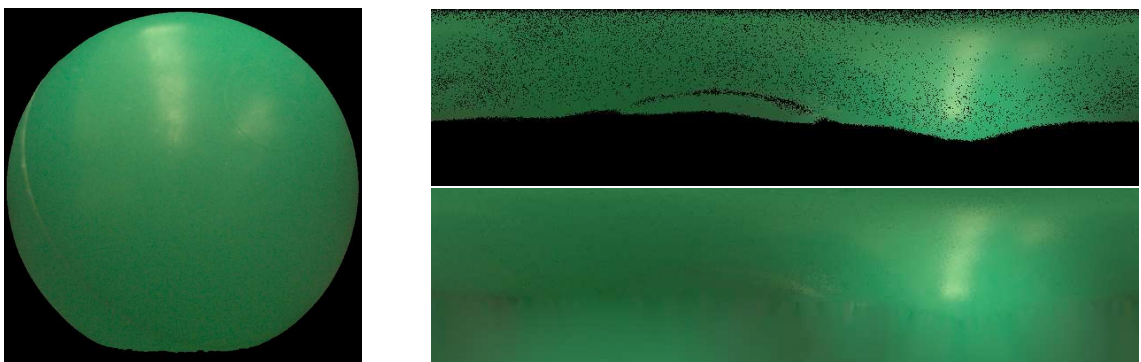


Figure 5.5: Left: Original natural image input; Top-Right: Original collected reflectance radiance map for hemisphere (green plastic ball). Bottom-Right: Interpolated result to which novel surface normal directions can be attributed.

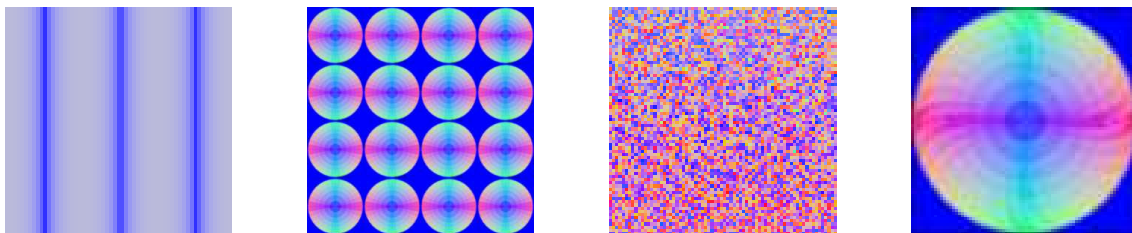


Figure 5.6: Examples of stamps (depicted as surface normals encoded in RGB) in the system: waves, bumps, random (within a hemisphere of angles), and a concave dimple, respectively. (Not pictured but also available: blurring and sharpening.)

Reflectance Look-up

After the user applies the stamp, the system automatically processes the warped boundaries of the selected region and rotates the underlying normals, one by one. To preserve the underlying mesostructure of the surface and yet perturb the surface according to the stamp, a quaternion rotation is built that composes the initial rotation of the normal (rotated from the canonical direction) with the desired rotation dictated by the stamp. This step is critical to the photo-realism of the result. Finally, the system updates the reflectance in this region by searching for each of the warped normals in the reflected radiance map.

When the system initially collects the original set of observed, reflected radiance values on the target object, these values represent a direct sampling of the interaction between the global illumination in the scene and the material that comprises our target object. In other words, some or all of the multi-bounce, indirect lighting and interreflectance illumination in the scene is factored into the visible reflected radiance at each point. Therefore, it is prudent to try to quantify this complex, secondary contribution of reflectance.

Consider the example of wanting to edit a cube comprised of a homogeneous material, with moderate gloss to its finish. This glossiness, paired with the lighting in the scene (however distant it might be), will create variation in reflectance across the surface of the cube. Now, imagine that there is a multitude of objects also in the scene with the target cube. The contribution of multiple bounces of light, reflecting off of these objects and back onto the cube will further confound the heterogeneity of reflectance across the surface.

For one surface normal at a location on a face of the cube, its reflectance might vary, because of this global illumination contribution, from a different portion of that face that points in the same direction. Which color should a pixel be that, once edited, takes on the value of this normal? Hence, we created a global illumination scale factor to compensate for this difference.

Global Illumination Correction

The scale factor typifies the average contribution of global illumination for this particular surface normal direction. Once we have the collated lists of surface normal directions and image locations to which they map, we take the average pixel value of each color-channel for all of these image locations, per normal. For each valid pixel that could be edited, this factor is calculated by dividing from the original pixel value this average RGB value for all matching normals, and it is recorded for later use. Upon editing, the value at the image position of the *current* pixel being edited is divided by the scale factor for this position; then the scale factor of the pixel value that is closest, in Euclidean distance, will be multiplied at the current position.

The editing of the normals may result in new normals that have either been observed originally in the target image or for which the system has interpolated values. To update the reflectance of the edited region, the system conducts a look-up of the normal: if there has only been one observation of a radiance value for this normal direction, the value is copied in; however, if multiple candidate values exist for this direction, the value for which its image location is closest, in Euclidean distance, to the image location of the current pixel is chosen. Finally, the global illumination correction factor is multiplied to the reflectance at this pixel location, as previously detailed. The system proceeds until the entire region is updated, and finally the border of the edited region is feathered in using Laplacian blending.

Fig. 5.7 shows screenshots of the editing application. It first presents the user with the

normals of the object that she wishes to edit (top) After the user selects a drawing tool and clicks and drags to select a region on the image, a pop-up menu gives her options for the operation to perform on the underlying surface normals. If she chooses the stamp option (middle), then an additional sub-menu appears (bottom), giving the user the option of the type of stamp to apply. Then the system takes over, processing the edit as defined above, and the user can access the result as an image of the edited natural image, in a pre-defined location.

5.4 Results

The results of using our editing application reveal encompassing of many material-types and shapes as input. The benefit of considering reflectance in terms of the fully intertwined material and illumination is that, barring sharp geometric discontinuities and interreflections, the system is tolerant of a range of specularity. Here, we show examples of edits produced through the input of both simulated and real photographs.

The benefit of this tool is that it permits a stamping-action in a physically plausible way. Applying an editing tool to an image of an object with highly varying surface geometry produces realistic results. In Fig. 5.8, the wave stamp is applied to the right portion of a simulated object, over the edge of the "window" and around the side of the sphere-like portion. The stamp successfully appears to curve around the corner. There is aliasing in the image, which can be attributed to the heavy shadowing present in the collected, reflected radiance; yet the edit is fairly robust. The high-frequency shadowing is most apparent in the interpolated reflected radiance map, seen in Fig 5.9. Varied geometry varies the shading across the surface, thereby presenting many possible candidate reflectance values to one normal. However, the candidate values closest in Euclidean distance are chosen. High-frequency shadows remain one weakness of the system, as evidenced by the aliasing.

Yet another interesting result is the velveteen bag, shown in Fig. 5.10. There is com-

plex shading, especially along the crimped neck of the bag. The dimple stamp creates a believable depression in the body of the bag, as well as on the crimped region, in the lower-left. The lower-right image also shows the dimple stamp applied but without the global illumination scaling factor applied. Without it, shadowing from competing surface normals in more shadowed regions of the bag dominates where it should not, defeating illumination consistency.

Subtle texture, along with preservation of overall surface variation can be captured in the edited region. For instance, in Fig. 5.11, the weave of the cotton is maintained through the application of the bump-stamp, in the top-right image. Furthermore, both effects, in combination, present themselves in the application of the same stamp but on the more ridge-like region of the object (lower-left image.) Without assigning importance to individual surface normal information for meso-structure level edits, this detail would be lost.

Relatively severe deformations are also possible, as depicted in Fig. 5.12. This glossy peapod exhibits specularity, depth discontinuity (at the edge where the pea and the pod meet), and highly varying surface normals. When the dimple stamp is applied to the surface of this object, it not only creates a believable, hemispherical depression in the object, but it also takes into account the depth-edge and its associated shadowing.

On more specular input, such as the aluminum in Fig. 5.13, the editor's dimple stamp also produces a convincing edit to the natural image. The convex depression of the stamp contains a highlight due to the new orientation of the surface at that point. The edit does, however, reveal noise. This is due to the fact that the new normals have not been observed in the input image. High frequency input, like the shiny object at hand, does not interpolate as smoothly as a more diffuse object would, with the same geometry.

These results demonstrate a flexible underlying system that produces strong results even when the application is presented with a variety of textures and glossiness as input. As long as the input does not exhibit significant regions of self-shadowing or contain interreflecting heterogeneous regions or other objects, the result is photorealistic.

5.5 Discussion & Limitations

For this work, we are motivated by increased interest in computer-aided editing of photorealistic environments. In undertaking this problem ourselves, we recognize the importance of maintaining photorealistic fidelity yet facilitating ample user-exploration. Given that this system only mimics three-dimensionality, it is a simulation of real data, by default. However, we provide tools that function within realistic constraints of this simulation, namely, that the visible, edited surface normals cannot inherit values that extend beyond the angle of view of the camera.

It follows that the more surface normals the object contains, the better range of angular information there is of both the object's material and the irradiance environment map. In the worst case scenario, the object is completely flat, exhibiting one surface normal value. This would obviously be a pointless seed for the interpolated reflected radiance map. Even cubes are a poor starting point. The quality of the system's result is highly dependent on the angular complexity of the input.

On the other hand, if the object exhibits too good of an angular sampling of the irradiance map - in other words, if it is highly specular - then this variance would make ambiguous the relationship between surface orientation and the final reflected radiance value. This is especially a problem if multiple (completely disparate) radiance values map to the same surface normal. The problem worsens as object shape becomes less complex, yet is very specular.

The system also suffers in the presence of input that contains high-frequency *shadowing* or overt interreflectance. This is because the scaling term that we apply to compensate for shadows only serves to correct for slowly varying change in luminance. Otherwise, a stark change in reflectance is assumed to be either part of the heterogeneous material of the object or the non-uniformity of the distant lighting. Currently, it is the responsibility of the user to recognize when a target object is exhibiting any of these conditions and to expect that the system has already attempted to incorporate these phenomena into the

interpolated reflected radiance map. Therefore, certain edits will incorporate inaccurate reflectance information.

The realism of the results is also only as accurate as the estimation of the surface normals, of course. As one can see in Fig. 5.14, the blue bag, in fact, has a fold or ridge towards the top. It is a depth discontinuity, and the negligible shading difference along it is not strong enough to be detected by the photometric stereo algorithm. Consequently, it is a region in which the opportunity to withdraw reflectance information is lost, whether or not the user realizes it. This system has great potential for continued development, integrating compensation techniques for more challenging or more arbitrary input.

5.6 Conclusion

We have demonstrated our system, an image-based editor that mimics three-dimensional manipulation of surface mesostructure. It enables a user, even a novice graphic artist, to apply surface normal perturbation "stamps" to alter the surface texture of an object in a photograph. Our system is robust to diffuse, glossy, and moderately shadowed target objects. We have not yet incorporated the ability to import highly complex scenes, crowding the target object and forcing significant interreflectance. With the system's continued use, we expect to gain feedback for the most useful direction to take for potential improvements.

A desired follow-up study to this investigation is establishing the per-normal relationship between two different materials under the same illumination. In other words, a powerful addition to the tool would be a swapping mechanism by which the user could edit multiple objects in the same scene and have the ability to swap materials between objects. The difficulty is in avoiding shadowed and interreflected regions while trying to establish the transfer function. This study would be a promising future project, based on this editing application.

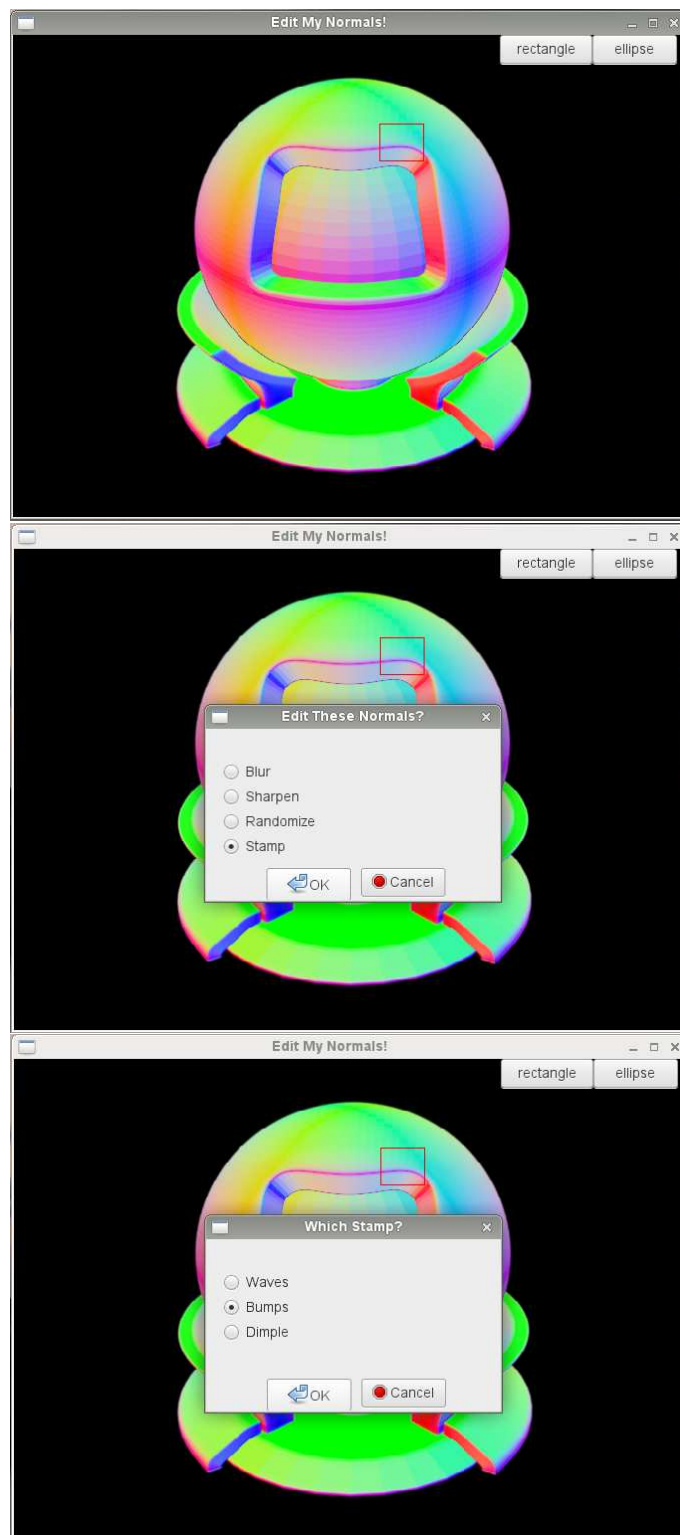


Figure 5.7: Screenshots of the editing application. Top: initial editing window, on which the user selects a region to edit. Middle: Editing tool pop-up menu. Bottom: The stamping sub-menu.

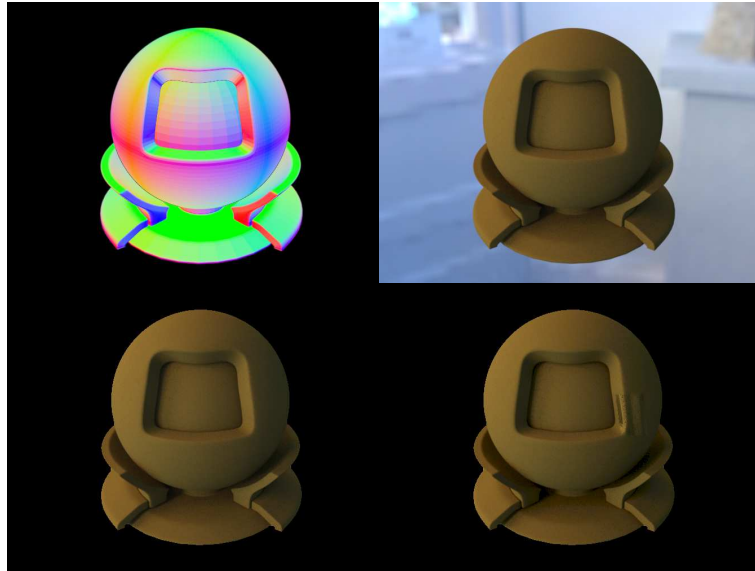


Figure 5.8: Top-Left: Surface normals of rendered, diffuse object. Top-Right: Object illuminated by environment map. Bottom-Left: Original input. Bottom-Right: Object stamped with waves, which bend around the corner. Rendering: Mitsuba [28].



Figure 5.9: Interpolated reflected radiance map for the brown, diffuse object. Note the black spots scattered throughout, due to the high-frequency shadowing introduced by the object's self-shadowing geometry.

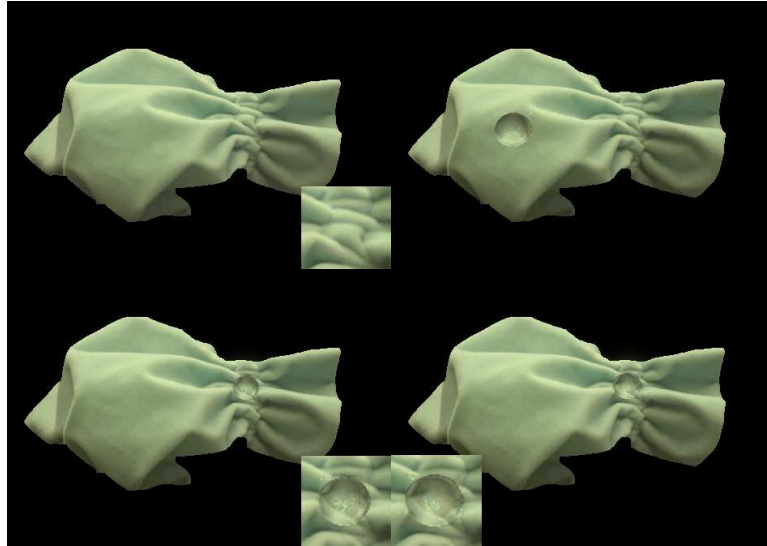


Figure 5.10: Top-Left: Original input of a velveteen bag, inset is a close-up of the original crimped region. Top-Right: Dimple stamp applied to flat portion of input, causing an apparent impression in the surface. Bottom-Left: Dimple stamp also applied to crimp in the bag neck. Notice how the crimping is preserved underneath. Bottom-Right: Dimple applied to the same region on the crimp, this time without global illumination scaling factor. Notice the excessive shadowing introduced.



Figure 5.11: Top-Left: Original input of a pink, cotton sock. Top-Right: Bump stamp applied to flat portion of input, causing apparent bumps in the surface. Bottom: Bump stamp also applied to ridge of sock.

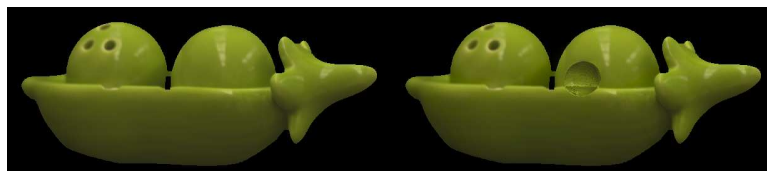


Figure 5.12: Left: Original input of a glossy peapod figure. Right: Dimple stamp applied to input. Notice that the depth-edge is included in the depression, as well as the shadowing associated with such a discontinuity.

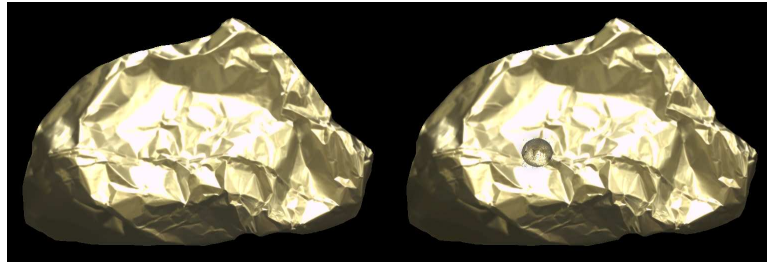


Figure 5.13: Left: Original input of crumpled ball of aluminum. Right: Dimple stamp applied to input. Notice that the underlying, complex geometry is still preserved.

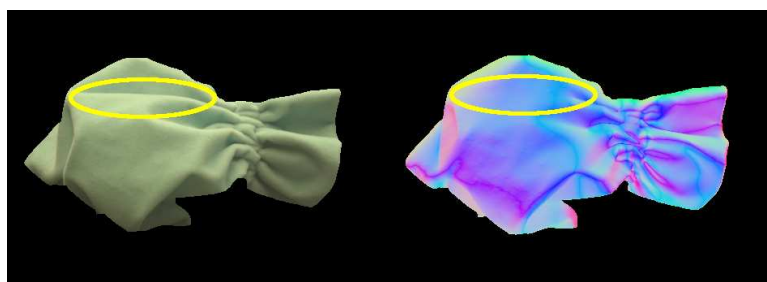


Figure 5.14: The blue bag exhibits a fold or ridge (left) that is not detected in the normals (right.)

Chapter 6

Conclusion

In this dissertation, we have investigated, from multiple directions, the distinct impact that surface normals have on an object's appearance. We present experiments and tools that reveal the seemingly subtle properties that can actually have an impressive effect on surface orientation measurement and appearance. Sometimes these parameters can even convince the viewer that certain textural properties are inherent to an object's material. Refining and perturbing these parameters can be done through both the manipulation of the factors that dictate an material's translucency, or alternatively, manipulation of its surface normals.

These three projects - the empirical study of photometric stereo, subsequent surface normal refinement, and the reflected radiance appearance editor - underscore the depth of information encoded in photographs. Because our visual system can tolerate slight inaccuracies in appearance estimation and yet can also be extremely critical about appearance, the tolerance-level of an object's digitized appearance depends on the desired application. Perhaps the illusion of translucency is actually desired. Perhaps the application only requires an estimate of the general shape of an object, and neither microgeometric- nor mesostructural-level accuracy is necessary.

The digitized world is only as realistic as our methods of rendering it, and there is a wealth of ways in which we can do so. We have to choose wisely and take into account

what information we can extract about the properties of objects of interest. Future work in broadening how important surface normal measurement and mesostructural perturbations are to many *more* algorithms and assumptions, is an exciting opportunity. We hope to continue projects in this area, especially stemming from the latter two projects, pushing these experiments to the limit. For the surface-normal refinement: how curved of a surface is really tolerable for recovering ground truth normals? For the mesostructure editor: how can we transfer appearance, still keeping in mind that unknown reflectance in certain directions must be inferred? The three-dimensional world of infinitesimal shapes and their appearances is captured in photographs, locked within. This information is ours for the taking.

Bibliography

- [1] N. Alldrin and D. Kriegman. Toward reconstructing surfaces with arbitrary isotropic reflectance: A stratified photometric stereo approach. In *Proc. Int. Conf. Computer Vision*, pages 1--8, 2007.
- [2] Jonathan T Barron and Jitendra Malik. Shape, illumination, and reflectance from shading. *Pattern Analysis and Machine Intelligence, IEEE Transactions on*, 37(8):1670--1687, 2015.
- [3] S. Barsky and M. Petrou. The 4-source photometric stereo technique for three-dimensional surfaces in the presence of highlights and shadows. *IEEE Trans. Pattern Anal. Mach. Intell.*, 25(10):1239--1252, 2003.
- [4] R. Basri and D. Jacobs. Photometric stereo with general, unknown lighting. In *Proc. Conf. Computer Vision and Pattern Recognition*, pages 374--381, 2001.
- [5] Blender Online Community. Blender - a 3d modelling and rendering package, 2016.
- [6] G. Bradski. *Dr. Dobb's Journal of Software Tools*, 2000.
- [7] Brian Cabral, Marc Olano, and Philip Nemec. Reflection space image based rendering. In *Proceedings of the 26th annual conference on Computer graphics and interactive techniques*, pages 165--170. ACM Press/Addison-Wesley Publishing Co., 1999.
- [8] CatherineMunro, 2016.

- [9] Paul Debevec. Light probe image gallery, April 2014.
- [10] E. D'Eon and G. Irving. A quantized-diffusion model for rendering translucent materials. *ACM Trans. Graph*, 30(4):56:1--56:14, July 2011.
- [11] Olga Diamanti, Connelly Barnes, Sylvain Paris, Eli Shechtman, and Olga Sorkine-Hornung. Synthesis of complex image appearance from limited exemplars. *ACM Transactions on Graphics (TOG)*, 34(2):22, 2015.
- [12] C. Donner and H. W. Jensen. Light diffusion in multi-layered translucent materials. *ACM Trans. Graph*, 24(3):1032--1039, 2005.
- [13] C. Donner, J. Lawrence, R. Ramamoorthi, T. Hachisuka, H. W. Jensen, and S. K. Nayar. An empirical bssrdf model. *ACM Trans. Graph.*, 28(3), 2009.
- [14] Craig Donner, Tim Weyrich, Eugene d'Eon, Ravi Ramamoorthi, and Szymon Rusinkiewicz. A layered, heterogeneous reflectance model for acquiring and rendering human skin. In *ACM TOG (Proceedings of SIGGRAPH Asia)*, 2008.
- [15] Hui Fang and John C Hart. Detail preserving shape deformation in image editing. In *ACM Transactions on Graphics (TOG)*, volume 26, page 12. ACM, 2007.
- [16] Abhijeet Ghosh, Tim Hawkins, Pieter Peers, Sune Frederiksen, and Paul Debevec. Practical modeling and acquisition of layered facial reflectance. *ACM Transactions on Graphics*, 27(5):139:1--139:10, December 2008.
- [17] Loeiz Glondu, Lien Muguercia, Maud Marchal, Carles Bosch, Holly Rushmeier, Georges Dumont, and George Drettakis. Example-based fractured appearance. In *Computer Graphics Forum*, volume 31, pages 1547--1556. Wiley Online Library, 2012.
- [18] G. Godin, J.-A. Beraldin, M. Rioux, M. Levoy, L. Cournoyer, and F. Blais. An assessment of laser range measurement of marble surfaces. In *Proc. Fifth Conference on optical 3-D measurement techniques*, 2001.

- [19] M. Goesele, H. P. A. Lensch, J. Lang, C. Fuchs, and H.-P. Seidel. Disco: acquisition of translucent objects. *ACM Trans. Graph.*, 23(3):835--844, August 2004.
- [20] D. B. Goldman, B. Curless, A. Hertzmann, and S. M. Seitz. Shape and spatially-varying brdfs from photometric stereo. In *Proc. Conf. Computer Vision and Pattern Recognition*, pages 341--348, 2005.
- [21] Ralf Habel, Per H Christensen, and Wojciech Jarosz. Photon beam diffusion: A hybrid monte carlo method for subsurface scattering. In *Computer Graphics Forum*, volume 32, pages 27--37. Wiley Online Library, 2013.
- [22] P. Hanrahan and W. Krueger. Reflection from layered surfaces due to subsurface scattering. In *Proc. SIGGRAPH 93*, pages 165--174, 1993.
- [23] Aaron Hertzmann, Charles E Jacobs, Nuria Oliver, Brian Curless, and David H Salesin. Image analogies. In *Proceedings of the 28th annual conference on Computer graphics and interactive techniques*, pages 327--340. ACM, 2001.
- [24] M. Holroyd and J. Lawrence. An analysis of using high-frequency sinusoidal illumination to measure the 3d shape of translucent objects. In *Proc. Conf. Computer Vision and Pattern Recognition*, pages 2985--2991, 2011.
- [25] M. Holroyd, J. Lawrence, and T. Zickler. A coaxial optical scanner for synchronous acquisition of 3d geometry and surface reflectance. *ACM Trans. Graph.*, 29(4), 2010.
- [26] Robert Hooke and T. A. Jeeves. "direct search" solution of numerical and statistical problems. *J. ACM*, 8(2):212--229, April 1961.
- [27] C. Inoshita, Y. Mukaigawa, Y. Matsushita, and Y. Yagi. Shape from single scattering for translucent objects. In *Proc. European Conf. Computer Vision*, pages 371--384, 2012.
- [28] Wenzel Jakob. Mitsuba renderer, 2010. <http://www.mitsuba-renderer.org>.

- [29] H. W. Jensen, S.R. Marschner, M. Levoy, and P. Hanrahan. A practical model for subsurface light transport. In *Proc. SIGGRAPH 2001*, pages 511--518, 2001.
- [30] James T Kajiya. The rendering equation. In *ACM Siggraph Computer Graphics*, volume 20, pages 143--150. ACM, 1986.
- [31] Jan Kautz, Solomon Boulos, and Frédo Durand. Interactive editing and modeling of bidirectional texture functions. In *ACM Transactions on Graphics (TOG)*, volume 26, page 53. ACM, 2007.
- [32] Erum Arif Khan, Erik Reinhard, Roland W Fleming, and Heinrich H Bülthoff. Image-based material editing. In *ACM Transactions on Graphics (TOG)*, volume 25, pages 654--663. ACM, 2006.
- [33] Pierre-Yves Laffont, Zhile Ren, Xiaofeng Tao, Chao Qian, and James Hays. Transient attributes for high-level understanding and editing of outdoor scenes. *ACM Transactions on Graphics (TOG)*, 33(4):149, 2014.
- [34] W. Ma, T. Hawkins, P. Peers, C. Chabert, M. Weiss, and P. Debevec. Rapid acquisition of specular and diffuse normal maps from polarized spherical gradient illumination. In *Proc. Eurographics Symposium on Rendering*, 2007.
- [35] Wojciech Matusik, Hanspeter Pfister, Matt Brand, and Leonard McMillan. A data-driven reflectance model. *ACM Transactions on Graphics*, 22(3):759--769, July 2003.
- [36] K. Moore and P. Peers. An empirical study on the effects of translucency on photometric stereo. *The Visual Computer*, 29(6), 2013.
- [37] S. K. Nayar, K. Ikeuchi, and T. Kanade. Determining shape and reflectance of lambertian, specular, and hybrid surfaces using extended sources. In *International Workshop on Industrial Applications of Machine Intelligence and Vision*, pages 169-175, 1989.

- [38] S. K. Nayar, G. Krishnan, M. D. Grossberg, and R. Raskar. Fast separation of direct and global components of a scene using high frequency illumination. *ACM Trans. on Graphics*, 25(3):935--944, 2006.
- [39] D. Nehab, S. Rusinkiewicz, J. Davis, and R. Ramamoorthi. Efficiently combining positions and normals for precise 3d geometry. *ACM Trans. on Graphics*, 24(3):536--543, 2005.
- [40] F. E. Nicodemus, J. C. Richmond, J. J. Hsia, I. W. Ginsberg, and T. Limperis. Geometric considerations and nomenclature for reflectance. *National Bureau of Standards Monograph 160*, 1977.
- [41] Pieter Peers, Karl vom Berge, Wojciech Matusik, Ravi Ramamoorthi, Jason Lawrence, Szymon Rusinkiewicz, and Philip Dutré. A compact factored representation of heterogeneous subsurface scattering. *ACM TOG*, 25(3):746--753, 2006.
- [42] Bui Tuong Phong. Illumination for computer generated pictures. *Communications of the ACM*, 18(6):311--317, 1975.
- [43] Ganesh Ramanarayanan, James Ferwerda, Bruce Walter, and Kavita Bala. Visual equivalence: towards a new standard for image fidelity. *ACM Transactions on Graphics (TOG)*, 26(3):76, 2007.
- [44] Peter-Pike J Sloan, William Martin, Amy Gooch, and Bruce Gooch. The lit sphere: A model for capturing npr shading from art. In *Graphics interface*, volume 2001, pages 143--150. Citeseer, 2001.
- [45] J. Stam. Multiple scattering as a diffusion process. In *Proc. Eurographics Workshop on Rendering*, pages 41--50, 1995.
- [46] Tim Weyrich, Wojciech Matusik, Hanspeter Pfister, Bernd Bickel, Craig Donner, Chien Tu, Janet McAndless, Jinho Lee, Addy Ngan, Henrik Wann Jensen, and

- Markus Gross. Analysis of human faces using a measurement-based skin reflectance model. *ACM TOG*, 25(3):1013--1024, 2006.
- [47] Ryan White and David Forsyth. Retexturing single views using texture and shading. In *Computer Vision--ECCV 2006*, pages 70--81. Springer, 2006.
- [48] R. J. Woodham. Photometric method for determining surface orientation from multiple images. *Optical Engineering*, 19(1):3050--3068, 1980.
- [49] Tai-Pang Wu, Jian Sun, Chi-Keung Tang, and Heung-Yeung Shum. Interactive normal reconstruction from a single image. *ACM Transactions on Graphics (TOG)*, 27(5):119, 2008.
- [50] Yufeng Zhu, Pradeep Garigipati, Pieter Peers, Paul Debevec, and Abhijeet Ghosh. Estimating diffusion parameters from polarized spherical gradient illumination. *IEEE Computer Graphics and Applications*, 99, 2013.
- [51] Carlos J Zubiaga, Adolfo Munoz, Laurent Belcour, Carles Bosch, and Pascal Barla. Matcap decomposition for dynamic appearance manipulation. In *Eurographics Symposium on Rendering 2015*, 2015.